



HAL
open science

Exploring the Impact of Zeolite Porous Voids in Liquid Phase Reactions: The Case of Glycerol Etherification by tert-Butyl Alcohol

C Miranda, J Urresta, H Cruchade, A Tran, M Benghalem, A Astafan, P. Gaudin, T J Daou, A. Ramírez, Y Pouilloux, et al.

► To cite this version:

C Miranda, J Urresta, H Cruchade, A Tran, M Benghalem, et al.. Exploring the Impact of Zeolite Porous Voids in Liquid Phase Reactions: The Case of Glycerol Etherification by tert-Butyl Alcohol. Journal of Catalysis, 2018, 365, pp.249-260. 10.1016/j.jcat.2018.07.009 . hal-02352299

HAL Id: hal-02352299

<https://hal.science/hal-02352299>

Submitted on 6 Nov 2019

HAL is a multi-disciplinary open access archive for the deposit and dissemination of scientific research documents, whether they are published or not. The documents may come from teaching and research institutions in France or abroad, or from public or private research centers.

L'archive ouverte pluridisciplinaire **HAL**, est destinée au dépôt et à la diffusion de documents scientifiques de niveau recherche, publiés ou non, émanant des établissements d'enseignement et de recherche français ou étrangers, des laboratoires publics ou privés.

1 **Exploring the Impact of Zeolite Porous Voids in Liquid Phase**
2 **Reactions: The Case of Glycerol Etherification by *tert*-Butyl**
3 **Alcohol**

4
5 **C. Miranda^{ab}, J. Urresta^a, H. Cruchade^b, A. Tran^b, M. Benghalem^b, A. Astafan^b, P.**
6 **Gaudin^b, T. J. Daou^c, A. Ramírez^d, Y. Pouilloux^b, A. Sachse^{*b}, L. Pinard^{*b}**

7
8 ^a *Catalysis and Processes Research Laboratory (LICAP) - University of Valle, Meléndez*
9 *University City, Calle 13 # 100-00, Cali - Colombia.*

10 ^b *Institut de Chimie des Milieux et Matériaux de Poitiers (ICM2P), UMR 7285 CNRS, 4*
11 *Rue Michel Brunet, Bâtiment B27, 86073 Poitiers Cedex – France.*

12 ^c *Université de Haute Alsace, Université de Strasbourg, Axe Matériaux à Porosité*
13 *Contrôlée (MPC), Institut de Science des Matériaux de Mulhouse (IS2M), UMR CNRS*
14 *7361, ENSCMu, 3 bis rue Alfred Werner, 68093 Mulhouse Cedex – France.*

15 ^d *Catalysis Group, Department of Chemistry, University of Cauca, Carrera 3 No. 3N-100*
16 *Popayán-Colombia.*

17 ***Corresponding authors:** alexander.sachse@univ-poitiers.fr; ludovic.pinard@univ-
18 poitiers.fr

27 **Abstract**

28 The role of acidity (nature, concentration, strength) and textural properties in the
29 etherification of glycerol with *tert*-butyl alcohol was studied for a wide range acid catalysts,
30 such as Amberlyst[®] 15, silica, alumina, silica alumina and four type of zeolite, *i.e.* FAU,
31 MOR, *BEA and MFI. The etherification of glycerol by *tert*-butyl alcohol is a
32 thermodynamically limited reaction that occurs through a successive reaction sequence. We
33 found major evidence that glycerol etherification is not only a function of the amount of
34 Brønsted acid sites, but that it further proceeds via a product shape selectivity mechanism.
35 Indeed, the formation of di-substituted ethers appears at very low conversions for zeolites
36 compared to meso- and macroporous acid catalysts. *BEA and MFI zeolites feature similar
37 confining voids and resulting thus in similar intrinsic acid strengths (as proved by *n*-hexane
38 cracking), but differ in the connectivity (4 vs. 6 channels) and access to these voids (0.54
39 vs. 0.67 nm), which leads to diffusion issues, notably for the MFI zeolite.

40

41 *Key words:* glycerol etherification, zeolites, confinement effect, auto-inhibition effect,
42 Brønsted acidity, product shape selectivity.

43

44

45

46

47

48

49

50

51

52

53

54 **1. Introduction**

55 Glycerol is employed in over 1500 industrial applications and amounts to an annual
56 production of ca 160.000 tons [1]. By the year 2020, it is estimated that glycerol production
57 will exceed global demand by a factor of six [2]. Hence, the development of efficient
58 strategies for the glycerol conversion into value-added products represents a major issue as
59 far as glycerol disposal and the dealing with surplus production is concerned. A sustainable
60 strategy to valorize the polyol is its conversion into glycerol ethers, with widespread
61 applications, such as oxygenated fuel additives, intermediates in the pharmaceutical
62 industry, and non-ionic surfactants [3-5].

63 The etherification between two alcohols is promoted through acid catalysis. The use
64 of homogeneous catalyst such as strong acids (*e.g.* H₂SO₄) [6] represents major
65 inconveniences causing corrosion and environmental issues. Solid acid catalysts are an
66 indisputable mean to overcome these drawbacks. A prominent family of solid acid catalyst
67 are ion-exchanged resins. Yet, these resins present important limitations, such as low
68 surface area and a poor thermal stability [7]. Zeolites are a class of solid acids that feature
69 strong Brønsted acidity with high thermal and mechanical stability; making them very
70 promising solid catalysts for the glycerol etherification [7, 8].

71 González *et al.* [9] carried out the etherification of glycerol with *tert*-butyl alcohol
72 (TBA) at 348 K, on three commercial acidic zeolites: *BEA, MOR and MFI with
73 respective Si/Al molar ratios of 10, 6.5 and 20. The authors evidenced that *BEA zeolite
74 allowed to achieve highest conversion (75% with catalyst loadings of 5wt%) for this
75 transformation, which was further confirmed by others [10,11] and its activity can further
76 be improved through post-synthetic modifications, such as desilication (using alkaline
77 agents) and fluorination treatments [12]. Improved accessibility of Brønsted acid sites

78 allows for higher glycerol conversions and selectivities of di- and tri-substituted ethers. The
79 most efficient way to guarantee an important access of glycerol and *tert*-butyl alcohol to
80 protonic sites is to decrease the diffusion path length. Indeed, Simone *et al.* [13]
81 synthesized MFI based nanosponge and nanosheet, featuring structured hierarchical
82 systems of connected pores on different length scales. The authors observed, that the
83 hierarchical catalysts are both more active and selective towards the formation of higher
84 substituted ethers compared to the purely microporous ones.

85 The location of protonic sites within the pore system influences the catalyst activity,
86 selectivity and stability. This is particularly the case with zeolite materials where the size of
87 micropores is often close to those of reactant(s), product(s) and reaction intermediate(s),
88 which is at the origin of what is referred as molecular shape selectivity (MSS). MSS results
89 from constraints arising from the interaction of molecules or intermediates within the
90 zeolite channels or cages of molecular size [14-15]. Reactant or product selectivity can be
91 observed when reactant or product molecules diffuse at very different rates within the
92 zeolite micropores as a function of their sizes. Moreover, the formation of bulky transition
93 states can be limited or inhibited within cages or channel intersections (restricted transition
94 state selectivity). Despite, these constraints positive interactions (such as confinement,
95 solvation [16]) can further occur between reactant and intermediate molecules and the
96 intracrystalline zeolite pore volume, which affect the rates of catalytic reactions. Therefore,
97 the differences in activity of zeolite catalysts can result from the solvating characteristics of
98 their channels, channel intersections and cages.

99 The aim of this study is to evaluate the impact of the zeolite voids and void
100 interconnections on the activity, selectivity and stability of the liquid phase glycerol
101 etherification with *tert*-butyl alcohol. For this purpose, various types of solid acid catalysts,

102 such as Amberlyst[®] 15, silica, alumina, silica alumina and four series of zeolites (*i.e.* MOR,
103 FAU, *BEA and MFI) with diverse Si/Al molar ratios and morphologies were compared.

104 **2. Experimental section**

105 **2.1 Chemicals and catalysts**

106 Glycerol (99%) and *tert*-butyl alcohol (99.4%) were obtained from Acros Organics.
107 The commercial zeolites and silica were supplied from Clariant, Zeolyst, PQ zeolites and
108 Sigma-Aldrich (**Table A1 in the supporting information**). The catalysts which were
109 previously synthesized [17-22] and used in other studies are resumed in Table 1 and their
110 preparation procedure reported in the supporting information **section A.1** (catalyst synthesis
111 protocol).

112 **2.2 Characterization**

113 The structural characterization of the synthesized zeolites were carried out by X-ray
114 powder diffraction (XRD) on a PANalytical MPD X'Pert Pro diffractometer operating with
115 Cu K α radiation ($\lambda = 0.15418$ nm) and equipped with an X'Celerator real-time multiple
116 strip detector (active length = $2.122^\circ 2\theta$). The XRD patterns of the synthesized and
117 modified zeolites are shown in the supporting information (S.I. **Figure A2**).

118 The morphology, homogeneity and particle sizes were determined using a scanning
119 electron microscope (SEM) (Philips XL30 FEG). Samples were characterized by
120 transmission electronic microscopy (TEM) using a Philips CM 120 microscope equipped
121 with a LaB₆ filament. Nitrogen adsorption and desorption measurements were carried out at
122 77 K on a Micromeritics ASAP 2420 apparatus. Prior to analysis, the samples were
123 pretreated at 573 K under vacuum for 15 h. The specific surface area (S_{BET}) was calculated
124 according to the BET method in the relative pressure range of $2 \times 10^{-4} < p/p_0 \leq 8 \times 10^{-2}$ and
125 $4 \times 10^{-3} < p/p_0 \leq 12 \times 10^{-2}$ for microcrystals and hierarchical materials (nanosponges and

126 nanocrystals), respectively. The microporous volumes (V_{micro}) were calculated using the t -
127 plot method. The pore size distributions were determined using a density functional theory
128 (DFT) model applied on the adsorption branch. The total pore volume was calculated at
129 $p/p_0 = 0.9$. The mesopore volume (V_{meso}) were determined by the difference between the
130 total pore volume and the micropore volume.

131 The bulk silicon to aluminum molar ratio was determined by X-ray fluorescence
132 (XRF) spectrometry (Philips, Magic X). The framework silicon to aluminum molar ratio
133 was measured by ^{27}Al and ^{29}Si MAS NMR (spectra were recorded at 104.28 MHz on a
134 Bruker advance II 400 MHz spectrometer using a spinning rate of 12 kHz, a pulse length of
135 0.42 ls and a recycle time of 0.58 s) and estimated from infrared spectroscopy
136 measurements on a FT-IR Magna 550 Nicolet spectrometer. The position of the zeolite
137 structure bands (450–1250 cm^{-1}) allows the calculation of the framework aluminum content
138 using the correlation given in the literature in ref [23, 24]. The two techniques used on the
139 *BEA zeolites gave similar results (**Table 1**).

140 Fourier transform Infrared spectra (FT-IR) of pyridine adsorbed samples were recorded on
141 a Nicolet Magna 550-FT-IR spectrometer with a 2 cm^{-1} optical resolution. The zeolites
142 were first pressed into self-supporting wafers (diameter: 1.6 cm, $\approx 20 \text{ mg}$) and pretreated
143 from room temperature to 723 K (heating rate of 1.5 K min^{-1} for 5 h under a pressure of
144 $1.33 \cdot 10^{-4} \text{ Pa}$) in an IR cell connected to a vacuum line. Pyridine adsorption was carried out
145 at 423 K. After establishing a pressure of 133 Pa at equilibrium, the cell is evacuated at 623
146 K to remove all physisorbed species. The amount of pyridine adsorbed on the Brønsted and
147 Lewis sites is determined by integrating the band areas at respectively 1545 cm^{-1} and 1454
148 cm^{-1} and using the following extinction coefficients measured at 293 K: $\epsilon_{1545} = 1.13$ and

149 $\epsilon_{1454} = 1.28 \text{ cm mol}^{-1}$ (Calibration curves in the SI **Figure A1**). It is worth mentioning that
150 the values of the integrated molar extinction coefficients are close to those found by Dwyer
151 *et al.* [26], and differ from the typically applied values presented by Emeis [27] (*i.e.* $\epsilon_{1545} =$
152 1.67 and $\epsilon_{1445} = 2.22 \text{ cm mol}^{-1}$). The difference is due to the temperature at which the
153 spectra were recorded. In our case and that presented in ref. [26], they were reordered at
154 293 K, whereas in the publication of Emeis at 423 K. According to Shi and Zhang [28] and
155 Bauer *et al.* [29], the temperature dependence of extinction coefficient is represented by a
156 simple power law: $\epsilon = \epsilon(T_0) \left(\frac{T}{T_0}\right)^A$, where A is the temperature exponent and T_0 the
157 reference temperature. It is thus important to ensure for the accurate quantification of BAS
158 and LAS that spectra are recorded at same temperatures used for the determination of molar
159 extinction coefficients.”

160 Thermogravimetric analysis was carried out using a SDT Q600 by heating samples
161 under N_2/O_2 (4:1) with a ramp of $10 \text{ }^\circ\text{C}/\text{min}$ up to $900 \text{ }^\circ\text{C}$.

162 **2.3 Model reactions**

163 ***n*-hexane cracking** : the catalytic tests of the *n*- C_6 cracking were performed in a fixed-bed
164 catalytic reactor. 40 mg of samples was pretreated at 813 K under nitrogen flow for 12 h. *n*-
165 Hexane (99.99 % pure from Sigma Aldrich) was then diluted in nitrogen flow and injected
166 in the reactor at 813 K with a molar ratio of 9. The contact time was fixed to 0.04 s.
167 Injections were obtained using 6 ways valve (Valco Vici 1/16 " fitting) and analyzed in
168 GC450 gas Chromatography equipped with a $\text{Cp-Al}_2\text{O}_3/\text{Na}_2\text{SO}_4$ capillary column (50 m, 10
169 μm) coupled with a FID detector. With fixed-bed catalytic reactors, an exact estimation of
170 the initial activity required extrapolation at zero time-on-stream (TOS) of measurements
171 carried out at relatively short intervals of TOS (1-5 min). However, with an on-line

172 analysis, the interval is determined by the time of this analysis (22 min). The use of a
173 multiposition valve to store the samples allowed overcoming this inconvenience [30]. In the
174 absence of zeolite, the thermal cracking of n-hexane at 813K yielded to less than 0.5%
175 conversion.

176 ***Glycerol etherification with tert-butyl alcohol:*** etherification experiments were
177 performed in a batch reactor: a glass stirred autoclave (15 mL) equipped with a temperature
178 controller and a pressure gauge. For the etherification of glycerol with *tert*-butyl alcohol,
179 the composition of the reaction mixture was: 2.79 g of glycerol, 9.00 g of *tert*-butyl alcohol
180 (glycerol/*tert*-butyl alcohol molar ratio of 0.25) and constant catalyst loading of 7.5wt%
181 (referred to glycerol mass). Stirring was fixed for all experiments to 1200 rpm to avoid
182 external diffusion limitations. Zeolites were activated before testing at 473 K under reduced
183 pressure during 12 h and the Amberlyst[®] 15 (Acros Organics) was washed with methanol
184 and dried in vacuum at 333 K. The reaction temperature was fixed at 363 K and samples
185 were taken at different times for 10 h under autogenous pressure, which can reach up to 5
186 bar. The reaction products were analyzed by gas chromatography using a chromatograph
187 model Agilent Technologies 7820A equipped with an auto-sampler G4567A, DB-WAX
188 column and a FID detector and butanol (Sigma Aldrich) as internal standard. Analyses were
189 carried out with temperature program from 313 to 513 K (with a slope of 293 K min⁻¹), and
190 at the initial and final temperature was maintained for 5 min isothermally. Glycerol, MTBG
191 (3-*tert*-butoxy-1,2 propanediol and 2-*tert*-butoxy-1,3 propanediol) and DTBG (2,3-di-*tert*-
192 butoxy-1-propanol and 1,3-di-*tert*-butoxy-2-propanol) response factors were determined by
193 calibration performed with standards. MTBG and DTBG, which were not available
194 commercially, were isolated from the products of the etherification reaction by column
195 chromatography (1:9 Ethyl Acetate/petroleum ether) and identified by ¹H-NMR.

196 Glycerol conversion (%), product selectivity (%) and the molar yield (%), were calculated
197 using the following equations:

$$198 \quad \text{Glycerol conversion (\%)} = \frac{\text{moles of reacted glycerol}}{\text{moles of initial glycerol}} \quad (\text{eq.1})$$

$$199 \quad \text{Product selectivity (\%)} = \frac{\text{moles of obtained product}}{\text{total moles of product}} \quad (\text{eq. 2})$$

$$200 \quad \text{Molar yield (\%)} = \frac{\text{moles of obtained product}}{\text{moles of initial glycerol}} \quad (\text{eq. 3})$$

201 The carbon balance with respect to glycerol was 95- 97% for all the catalysts except with γ -
202 Al_2O_3 , which was lower than 90%.

203 ***Catalyst regeneration and catalytic recycling:*** after stopping reactions, catalysts
204 were separated from reaction medium by centrifugation and spent catalysts were rinsed
205 with 55.8 mL ethanol at 373 K under 10 MPa nitrogen pressure during 14.5 min using a
206 Dionex ASE 350. The recovered rinsing solution was concentrated by evaporation on a
207 rotavap and characterized by gas chromatography. The amount of confined organic
208 molecules (after rinsing) was inferred through thermogravimetric analysis. Rinsed catalysts
209 were used directly or after calcination (773 K/8 h) in catalytic recycling experiments by
210 applying the protocol described above.

211 **3. Results and discussion**

212 **3.1. Catalyst characterization**

213 **Table 1** reports the textural and the acidic properties, the crystal size and the bulk
214 and the framework Si/Al molar ratios of the commercial and synthesized acidic catalysts.
215 Catalysts are designated as follows: the type of zeolite is indicated in brackets by using the
216 IZA structural code, the range of crystal size is indicated as subscript, *i.e.*, MC, SC, NC for

217 micrometer, sub-micrometer, nanometer-sized, and NSp, NSh for nanosponge and
218 nanosheet morphologies, respectively. The bulk Si/Al molar ratio is noted as superscript.

219 **Textural properties:** From nitrogen physisorption it was inferred that the silica,
220 alumina and silica-alumina exhibit almost no microporosity. The microporous volume of
221 zeolites (V_{micro}) is a “fingerprint” of their framework type. Independently of their crystal
222 size (**Figure 1a, Table 1**), MOR, FAU, *BEA and MFI zeolites feature V_{micro} of 0.20, 0.30,
223 0.23 and 0.18 $\text{cm}^3 \text{g}^{-1}$, respectively, which are the volumes expected for conventional well
224 crystallized zeolites for these structures. Mesopores can either be of intracrystalline or
225 intergranular nature and mesoporous volume (V_{meso}) is a function of both crystal size and
226 shape. For the samples depicted in **Figure 1b** and **Table 1** crystal size decreases with
227 increasing mesoporous volume. Hence, V_{meso} is close to zero on conventional micrometer
228 zeolite samples.

229 **Figure 2** compares the SEM and TEM images of the MOR, FAU, *BEA and MFI
230 zeolites. (MOR) $_{\text{SC}}^{10}$ features crystals with a length ranging from 100 to 500 nm. The SEM
231 image of (FAU) $_{\text{SC}}^{2,6}$ displays large crystal ($600 < \phi < 1000 \text{ nm}$) with bipyramidal shape.
232 Further, the TEM micrograph of (FAU) $_{\text{SC}}^{17}$ presents large crystals ($\phi = 500 \text{ nm}$). As far as
233 (*BEA) $_{\text{MC}}^{15}$ is concerned a truncated bipyramidal shape with crystal sizes ranging from 6 to
234 10 microns can be deduced. (*BEA) $_{\text{SC}}^9$ features aggregated crystals with sizes ranging from
235 300 to 1500 nm. (*BEA) $_{\text{SC}}^{10}$, synthesized in alkaline medium at 423 K, consists of crystals
236 with a smaller diameter (100–700 nm). Pseudo-spherical crystals with an average size of
237 40 nm are present for (*BEA) $_{\text{NC}}^{15}$, the aggregation of the nanocrystals yield intercrystalline
238 mesopores. *BEA-type zeolite synthesized from a polyquaternary ammonium surfactant
239 exhibits a sponge-like morphology. These nanosponges are formed by randomly aggregated

240 nanoparticles delimited by ordered mesoporous channels. The corresponding TEM image
241 reveals nanometer-sized *BEA units with a short thickness (2 nm) separated by narrow
242 channels with a width of a few nanometers. (MFI)_{MC}⁴⁰ features crystals with a diameter of
243 250 nm. For (MFI)_{NC}⁴⁵ sample, the replacement of the conventional structure directing agent
244 (*i.e.* TPAOH) by a bifunctional organic compound allowed for the formation of lamellar
245 materials, referred as nanosheets. The overall thickness of the lamellar stacking of
246 nanosheets is approximately 20-40 nm, whilst the thickness of individual nanosheets
247 corresponds to 2 nm. The increase of the carbon chain length and the number of quaternary
248 ammonium centers in the structuring agent (C₁₈₋₆₋₆₋₁₈) leads to a nanosponge morphology
249 (sample (MFI)_{NSp}²⁰), with nanocrystal sizes ranging from 3.7 to 4.6 nm, with uniform
250 distribution.

251 ***Acidic properties:*** A portion of the sulfonic acid groups on the Amberlyst[®] 15 (A-
252 15) are strong enough to protonate and retain pyridine at 423 K. The concentration of the
253 Brønsted acid sites (BAS) amounts to 2300 $\mu\text{mol g}^{-1}$, which corresponds to half of
254 exchange capacity (between Na⁺ and H⁺) provided by the Rohm & Hass (4.7 mmol g⁻¹).
255 This result corresponds well to earlier reports [31], where acid site density on the dry
256 macroreticular resin was measured from calorimetry of NH₃ at 353 K. The dry alumina
257 catalyst has only Lewis acid sites (321 $\mu\text{mol g}^{-1}$) while the SiO₂ based material features no
258 acidity able to retain pyridine at 423 K. Yet, the silica-alumina material features some BAS
259 (43 $\mu\text{mol g}^{-1}$). For the zeolites, the BAS concentration depends on both the Si/Al molar
260 ratio and on their accessibility. For instance, in the case of FAU type zeolites BAS located
261 within the sodalite cages are not accessible by pyridine and do not amount to the bulk
262 probed acidity. Hence, the ratio between the probed acid sites to the theoretical, calculated

263 from the elemental composition of the zeolite ($[\text{PyH}^+]_{423\text{K}}/[\text{H}^+]_{\text{Theoretical}}$) depends strongly on
264 the zeolite framework (**Figure 1c**). This ratio is low for FAU type zeolite and 0.8 for MOR,
265 due to acid sites located on the sodalite cages and side pockets, which are inaccessible to
266 the basic probe. On *BEA and MFI zeolites, the portion of acid sites that are able to retain
267 pyridine further depends on the average crystal size and $[\text{PyH}^+]_{423\text{K}}/[\text{H}^+]_{\text{Theoretical}}$ decreases
268 drastically with the crystal size. Yet, Ryoo *et al.* observed slight or no change in BAS
269 concentration with crystal downsizing [32,33]. They evidenced that a nanospongenous
270 *BEA zeolite (20 nm) contained 7 times more BAS at the external surface compare to a
271 micron-sized *BEA (2 μm) [32], and almost 9 times more on MFI-based nano-sheets (2
272 nm) than on large MFI crystals (> 300 nm) [33]. The same research group moreover
273 concluded from various catalytic tests, such as Friedel-Crafts alkylation of benzene, *n*-
274 octane cracking, Claisen-Schmidt condensation and methanol to DME conversion, that the
275 external BAS are weaker than those within the sheets (*i.e.* internal BAS). This suggests
276 that, the local geometry of protonic sites has a major impact on their activity since the
277 intrinsic strength of protonic sites, as demonstrated by Bokhoven *et al.* [34], is identical
278 regardless of the zeolite framework.

279 The amount of EFAL sites per unit cell can be concluded through comparing the
280 bulk and the framework Si/Al molar ratios. The quantity of EFAL sites is very high on
281 aluminum rich zeolite, such as FAU, which can easily be removed by thermal treatment
282 (essentially for FAU with a low Si/Al ratio) [35]. The presence of EFAL species can
283 generate Lewis acid sites (LAS). *BEA zeolite features an important portion of LAS (176 –
284 490 $\mu\text{mol g}^{-1}$) amounting to the total acidity. The total concentration of Lewis acid sites
285 increase with the number of EFAL species. Yet, this correlation is not perfectly linear (**SI.**

286 **Figure A.3)** as not all of the EFAL species comprise LAS and can be of cationic or neutral
287 nature, such as $\text{Al}(\text{OH})_2^+$, $\text{Al}(\text{OH})^{2+}$, AlO^+ , Al^{3+} , $\text{AlO}(\text{OH})$, pseudoboehmite and Al_2O_3
288 [36,37]. Moreover EFAL species can be located within or at the outer surface of the zeolite
289 microporosity.

290 **3.2 *n*-Hexane cracking**

291 The acidic properties of the mesoporous silica-alumina and zeolites (FAU, *BEA, MOR
292 and MFI) can be characterized by using the α test developed by Mobil almost 40 years ago
293 (*i.e.* *n*-hexane cracking at 813 K) [38]. In **Figure 3** $-\ln(1-X)$ is plotted as a function of
294 W/F , where X is the initial conversion, W represents the moles of Brønsted acid sites in the
295 reactor and F is the total volumetric flow rate at the reaction temperature (813 K). The
296 activity plot carried out on the medium pore zeolite with large crystals ((MFI)_{MC}⁴⁰) shows
297 that the *n*-hexane conversion follows a first-order kinetic model. The main mechanism that
298 initially occurs in our operating conditions (813, K, $P_{n-C_6} = 10$ kPa) is monomolecular. The
299 bimolecular route (*i.e.* autocatalysis) seems limited even with a high partial pressure of *n*-
300 hexane. Independently of the zeolite framework and crystal size, the *n*-hexane cracking
301 yields C_1 , C_2 , C_3 , C_4 , C_5 hydrocarbons, which are formed in strictly parallel reactions, and
302 relies on a monomolecular cracking mechanism (**SI. Figure B1**). The initial molar ratios
303 for C_5/C_1 , and C_4/C_2 (without discriminate between olefin and paraffin) on the different
304 catalysts are shown in (**SI. Figure B2**) as a function of the initial conversion. On all
305 zeolites, except on the nano-sponges and sheets, C_4/C_2 ratios are 0.75, which is slightly
306 lower than those reported by Babitz *et al.* [39] and Lercher *et al.* [40], which amount to 1-
307 0.8 and 0.8, respectively. While the C_5/C_1 ratios are significantly lower than unity, *i.e.*
308 about 0.3, they are consistent with the results reported in references [39] and [40]. These

309 ratios below unity indicate the occurrence of secondary cracking. Since the catalytic
310 behavior is identical for all solid acids investigated in the study, we assume that the main
311 kinetic regime involved in *n*-hexane cracking is mainly monomolecular. It should be noted
312 that the most active catalysts deactivate rapidly (**SI. Figure B3**); The deactivation is due to
313 the formation of coke. Its kinetics increase with the partial pressure of olefins (P_0): the
314 higher the conversion, the higher P_0 . Moreover, the partial pressure of *n*-hexane (P_{nC6}) is 25
315 to 100 higher than that used by Babitz *et al.* [39]. Therefore, in their operating conditions,
316 no deactivation occurs.

317 The initial activity is linear to the concentration of BAS probed by pyridine except
318 for $(FAU)_{SC}^{2.6}$, $(*BEA)_{NC}^{12.5}$ and $(*BEA)_{SC}^9$ (**Figure 4**), which feature a large amount of EFAL
319 species (**Table 1**). The higher activity on these three zeolites was ascribed to the presence
320 of EFAL through an exaltation of BAS strength [41-43]. Indeed, a study that combined
321 MAS NMR with DFT calculations evidenced the existence of a definite interaction between
322 the Brønsted and Lewis acid sites (LAS), which leads to an increase of the acid site strength
323 in the zeolite framework [44]. Yet, the presence of these "super-acid" sites has been
324 controverted by Iglesia and co-workers [45], who suggested that the apparent increased
325 strength of the BAS would not result from electronic interactions with EFAL species, but
326 rather from a higher solvation effect of zeolite voids attributable to the occlusion of the
327 void space by extraframework Al residues.

328 Despite of a more important amount of LAS on MFI nanosheets (*i.e.* $(MFI)_{NSh}^{45}$)
329 compared to bulk MFI samples, the turnover rate is not exalted, which suggests that on the
330 nanosheets the EFAL species are located on the external surface and not within the
331 micropores.

332 The initial activity per Brønsted acid site (TOF) was plotted as a function of
333 crystallite size (L) multiplied with square root of initial activity: $L(A_0)^{0.5}$ (**Figure 5**), this
334 parameter corresponds to a measure of the diffusion constraint [46]. The TOF values (in
335 absence of acidity exaltation or higher solvation effect) are independent of both the zeolite
336 framework and the crystal size, which means that the Thiele modulus ($\phi_s=L \sqrt{k}/(\sqrt{D_e})$),
337 even on very large crystals ($L > 8000 \text{ nm}$), is ≤ 1 . Therefore, the effective diffusion (D_e) of
338 *n*-hexane at high temperature (813 K) within zeolite micropores, even with medium pores is
339 high. Indeed, the effective size of *n*-hexane (*i.e.* 0.43 nm) is lower than that of the pore
340 aperture of the MFI framework: 0.54 x 0.56 nm. Haag *et al.* [46] established that the rate
341 constant for cracking of *n*-hexane is proportional to the concentration active aluminum sites
342 in HZSM-5 and that it is independent of the crystal size (thus $\eta = 1$). The same authors
343 measured the diffusivity of linear hydrocarbons in a ZSM-5 at 811 K, which is $3 \times 10^{-4} \text{ cm}^2$
344 s^{-1} , and can drop by a factor 10^4 with branched structures [46].

345 The TOF value on the *BEA zeolite series (except for $(\text{*BEA})_{\text{SC}}^9$ and $(\text{*BEA})_{\text{NC}}^{12.5}$) is
346 identical and independent of the crystal size (*ca.* 360-370 h^{-1}). The TOF on zeolites (with
347 confined protonic sites) is more than 180 times higher than the one observed on silica-
348 alumina (featuring unconfined BAS, 2 h^{-1}) (**SI. Table B.1**). This finding was in the past
349 ascribed to a difference in the intrinsic BAS strength [45]. Yet, it has been evidenced that
350 the difference in activity is rather related to confinement and solvation effects within the
351 zeolite voids [47,48]. As demonstrated by Iglesia *et al.* [48], the strength of BAS in
352 microporous and mesoporous aluminosilicates is identical and the diverse reactivities and
353 selectivities of BAS can readily be attributed to the confining voids of different sizes and
354 connectivities [45]. The similar turnover rates on $(\text{MFI})_{\text{MC}}^{40}$ and *BEA zeolites suggest voids

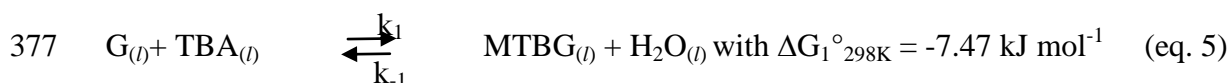
355 of similar size in these two frameworks. Indeed, for *BEA zeolite (**12MR** 5.5 x 5.5* ↔ 12
 356 7.6 x 6.4**) the pore-limiting diameter and the largest cavity diameter are 0.67 and 0.69
 357 nm, respectively, and on MFI zeolite ({**10MR** 5.3 x 5.6 ↔ 10 5.1 x 5.5}***), channel
 358 intersections lead to cage-like voids with a diameter of 0.70 nm. Iglesia *et al.* [49] observed
 359 for *BEA and MFI zeolites identical propene dimerization turnover rates regardless of the
 360 number of BAS per unit cell. The turnover rates are lower on sheet-like and nanospongy
 361 zeolites than on the bulk ones (**SI. Table B1**). This discrepancy is hence not attributed to a
 362 different intrinsic strength of the BAS but to the presence of more or less confined BAS.
 363 Therefore, assuming that the TOF is the sum of turnover rates of unconfined
 364 ($TOF_{SiO_2-Al_2O_3} = 2 \text{ h}^{-1}$) and confined acidic site ($TOF_{bulk} = 360 \text{ h}^{-1}$), it is possible to
 365 estimate the proportion of proton sites located within the microporosity:

$$366 \quad \text{Confined BAS (\%)} = \frac{TOF_{NSh \text{ or } NP} - TOF_{SiO_2-Al_2O_3}}{TOF_{bulk} - TOF_{SiO_2-Al_2O_3}} \times 100 \quad (\text{eq. 4})$$

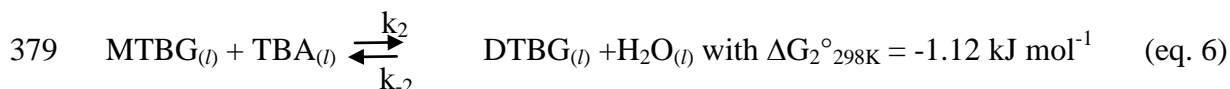
367 On (*BEA)¹⁷_{NSp}, (MFI)⁴⁵_{NSh}, and (MFI)²⁰_{NSp} the percentage of BAS in the microporous voids is
 368 63%, 41% and 22%, respectively. This result compares well to what has previously been
 369 reported by Ryoo *et al.*, who quantified the amount of external and internal BAS through
 370 probing with various probe molecules [32,33].

371 **3.3 Etherification of glycerol by *tert*-butyl alcohol**

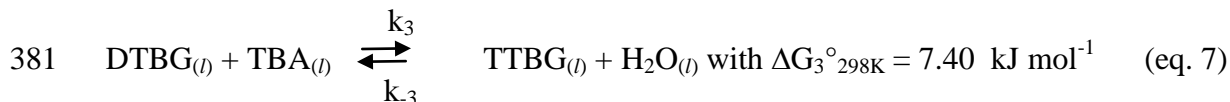
372 **Thermodynamic analysis of reaction equilibrium:** The glycerol etherification
 373 with *tert*-butyl alcohol was carried out in batch reactors at 363 K under autogenous pressure
 374 the reactions involved in the direct etherification of glycerol (G) and *tert*-butyl alcohol
 375 (TBA) in mono-, di- and tri- ethers (MTBG, DTBG and TTBG, respectively) are
 376 summarized as follows:



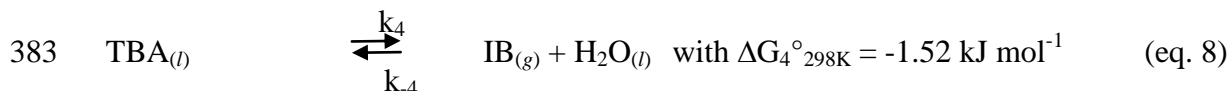
378



380



382



384

385 It is worth to mention that the reverse reaction of TBA dehydration is negligible,
386 since only a small amount of IB is dissolved in the liquid solution due to the low
387 autogenous pressure (<0.5 MPa). The standard Gibbs free energy of formation used for
388 MTBG, DTBG and TTBG are those obtained by Kiatkittipong [50] by using the Gani's
389 method [51] (**SI Table C1**). The authors predicted a minimization of the Gibbs free energy
390 for an equilibrium conversion of glycerol (X_{eq}) at 363 K (with a supposed equimolar
391 reactant mixture) of 75%. Pico *et al.* found from two simplified kinetic models at 363 K
392 with a TBA:G ratio of 1:4 (*i.e.* similar experimental condition to ours) a slightly higher
393 value of X_{eq} , *i.e.* 80% [52]. Hence, the etherification of glycerol and *tert*-butyl alcohol in
394 mono-, di- and tri-ethers is a reaction limited by a thermodynamic equilibrium, and in our
395 experimental conditions the maximum glycerol conversion expected is of 80%.

396 **Kinetic model:** The external mass transfer effect over $(\text{*BEA})_{\text{NC}}^{12.5}$ shows that the
397 conversion and selectivity into MTBG and DTBG increases with increasing stirring speed
398 and levels off at speeds higher than 800 rpm (**Figure 6**), indicating the absence of external
399 diffusion limitations at such stirring speeds. This results compare well to those obtained by
400 González *et al.* [12] and Karinen *et al.* [53], who observed a dependence of the product

401 selectivity as function of the stirring rate and that at higher speeds, the reaction was more
402 selective towards the ethers, while below 1000 rpm oligomerization of isobutylene was
403 observed. Therefore, the stirring speed has been set to 1200 rpm for all experiments.

404 The order of reaction for glycerol and *ter*-butyl alcohol were established on the
405 (*BEA)_{NC}^{12.5} catalyst at 363 K and estimated from the variation of the initial rate with the
406 concentration of that reactant, using the natural logarithm of the rate equation: $\ln r_0 =$
407 $\ln k + \alpha \ln[Gly]_0 + \beta \ln[TBA]_0$. The initial rate are measured in a series of experiments at
408 different initial concentration of Gly ranged from $2 \cdot 10^{-4}$ to $10 \cdot 10^{-4}$ mol cm⁻³ with a molar
409 ratio TBA/Gly from 10 to 40. In these conditions, the concentration of the exceeding
410 reactant can be considered as almost invariant. The slope of the straight line in **figure 7** of
411 $\ln r_0$ plot as a function of $\ln[Gly]_0$ then corresponds to the partial order with respect to Gly.
412 Similar experiments were carried out by maintaining the concentration of Gly constant and
413 varying that of TBA concentration from $4 \cdot 10^{-4}$ to $20 \cdot 10^{-4}$ mol cm⁻³. The partial kinetic
414 orders with respect to Gly and TBA are both close to 1. It is worth mentioning that for the
415 etherification on the solid-acid resin Amberlyst[®] 15, the kinetic orders found by Frusteri *et*
416 *al.* [54] are different and amount to an order of 0.3 with respect to Gly and an order of 1.7
417 with respect to *tert*-butyl alcohol. A possible explanation to this discrepancy might be due
418 to the ability of the macroporous resin to enable the kinetically relevant steps between
419 proximal adsorbates. Yet, Kiatkittipong *et al.* [50] found that on Amberslyst[®] 15 the
420 Langmuir-Hinshelwood (LH) activity based model is the best suited kinetic model to fit the
421 experimental results.

422 Nevertheless, a LH mechanism involving elementary steps between adsorbates on identical
423 sites is highly unlikely especially on high Si/Al zeolites due to the distance between two

424 adsorbates species (several nanometers). The coupling between such spatially dispersed
425 adsorbates to form C-O bonds in etherification is highly unlikely. Bimolecular reactions on
426 zeolites typically occur through Eley-Rideal (ER) type mechanisms, such as for alcohol
427 dehydration [55], alkane alkylation [56], olefin oligomerization [57] and aromatics
428 alkylation [58]. The partial kinetic orders with respect to glycerol and *tert*-butyl alcohol
429 concentration equal to 1 are consistent with an ER mechanism, where TBA reacts with the
430 adsorbed Gly.

431 **Activity and stability:** In **figure 8**, the glycerol conversion has been compared as a
432 function of the reaction time for following catalysts: Amberlyst[®] 15 (A-15 as reference
433 catalyst [7,59]), γ -Al₂O₃, SiO₂, SiO₂-Al₂O₃ and commercial zeolites ((MOR)_{NC}¹⁰, (FAU)_{SC}⁴⁰,
434 (*BEA)_{NC}^{12.5}, and (MFI)_{NC}⁴⁵). By employing A-15 as the catalyst, the conversion increases
435 rapidly and reaches a plateau at 64% within 1 h. The plateau is 16% lower than the
436 predicted equilibrium value, which means that conversion is hampered by deactivation of
437 the sulfonic resin, probably due to a product inhibition effect, *e.g.* by H₂O. The catalysts
438 based on SiO₂ and γ -Al₂O₃ show no catalytic activity for the etherification (**Table 2**).
439 Hence, glycerol etherification at 363 K requires protonic sites. It is to note that the Lewis
440 acid sites can catalyze the etherification reaction, yet merely at higher reaction temperatures
441 (T>473 K [59-60]). At low temperatures the alcohol remains strongly adsorbed on the
442 Lewis sites [61], thus yielding an incomplete carbon balance (< 90%). On silica-alumina
443 catalyst, the glycerol conversion is extremely slow and amounts to only 2% after 10 h of
444 reaction, ascribable to the low BAS concentration (43 μ mol g⁻¹). Employing (*BEA)_{NC}^{12.5}
445 allows to achieve an increasing conversion up to a pseudo-plateau lower than that of A-15
446 at approximately 54%.

447 Indeed, the rate decreases with time due to reactant consumption and accumulation of
448 products (MTBG) and more particularly water in the media. As there is no asymptotic
449 approach towards the value of glycerol conversion equilibrium, this suggests that the
450 catalysts deactivate (not by coking since the reaction temperature is too low, *i.e.* 353 K),
451 but through a product inhibiting effect [62]. Using (MOR)_{NC}¹⁰ a much stronger deactivation
452 is observed, achieving a plateau at only 6% after 1 h. Indeed, such mono-dimensional
453 zeolites are extremely sensitive to deactivation [63]. Employing (FAU)_{SC}⁴⁰ and (MFI)_{NC}⁴⁵ as
454 catalysts, the glycerol conversion increases continuously with the reaction time, yet after 10
455 h the conversions are considerably lower than on (*BEA)_{NC}^{12.5}, and are 33% and 20% against
456 54%, respectively (**Figure 8**). It is interesting to note that the catalytic behavior of both of
457 the large pores zeolites, FAU and *BEA, is significantly different. The higher efficiency of
458 *BEA could be due to either the small crystal size that favors the diffusion of reactant and
459 products or as proposed by Veiga *et al.* [64] to the hydrophobic/hydrophilic balance of its
460 surface. As far as the latter is concerned, the authors correlated catalytic activity and
461 hydrophobicity index (drawn from the non-competitive adsorption of water and toluene) for
462 FAU, MFI and *BEA zeolites. Yet, this relation is not consistent, as authors compared
463 zeolites featuring different crystal size, as suggested by the indicated external surface (S_{ext}).
464 Indeed, the high-value of S_{ext} of *BEA zeolite indicates small crystal size, whereas for FAU
465 and MFI zeolites, S_{ext} is low and corresponds hence to larger crystal sizes. Yet, the authors
466 found *BEA to be the most active catalyst among all tested zeolites.

467 Results of the catalytic etherification of glycerol with *tert*-butyl alcohol further
468 compared in terms of initial activity (A_0), where possible deactivation does not occur. A_0
469 was estimated from the slope of the tangent at zero time fitted to the curves presented in

470 **Figure 8.** The initial activity of the sulfonic resin A-15 is the highest due to the important
471 amount of BAS (**Table 2**). On the tridimensional zeolites with large pores, *i.e.* FAU and
472 *BEA zeolites, A_0 is proportional to the concentration of BAS, excepted for the catalyst
473 featuring large crystals, *i.e.* (*BEA)_{MC}¹⁵ and (FAU)_{SC}^{2,6}, that indicate the occurrence of
474 diffusion limitation (DL), (**Figure 9**).

475 The effectiveness factor (η) relates the observed reaction rate with the intrinsic
476 chemical rate ($r_{\text{obs}}/r_{\text{intrinsic}}$) and can be calculated from the ratio of two crystal sizes ($\frac{L_1}{L_2}$) and
477 the ratio of corresponding initial activities ($\frac{r_{A_1}}{r_{A_2}}$) by using an iteratively resolved algebraic
478 loop [65] (the method is detailed in **section C.M.2**). **Figure 10** reports η as a function of
479 the zeolite crystal size. The diffusion path being extremely short in *BEA nanosheets
480 (*BEA)_{NSp}¹⁷, no diffusion limitations occur ($\eta = 1$). DL occur on the *BEA zeolite with
481 crystal sizes above 100 nm. For the very acid MOR zeolite (1056 $\mu\text{mol g}^{-1} [\text{H}^+]$), activity is
482 very low due to the diffusion controlled reaction induced by the long diffusion path (crystal
483 size > 200 nm), and further accentuated by the mono-dimensional channel system.
484 Although *BEA and MFI zeolites have identical acid strength [34] and similar confining
485 voids (see section 3.2), the turnover rate is very low on the medium pore zeolite (9-46 h^{-1})
486 compared to that with large pores (150-198 h^{-1}). This suggests that diffusion limitations
487 occur even with a diffusion path length of a few nm. The DL is thus in this case most
488 importantly governed by zeolite pore size and the void connectivity. Indeed for *BEA the
489 void is connected by six 12 MR (0.67 nm), while for MFI by four 10 MR (0.54 nm). The
490 kinetic diameter of glycerol is 0.61 nm [66] that explains the diffusion limitation
491 encountered with the medium pore zeolite.

492 **Selectivity:** The etherification of glycerol with *tert*-butyl alcohol (TBA) proceeds
493 via a consecutive path that yields the formation of water and five different alkyl glycerol
494 ethers, which are MTBG (3-*tert*-butoxy-1,2 propanediol and 2-*tert*-butoxy-1,3
495 propanediol), DTBG (2,3-di-*tert*-butoxy-1-propanol and 1,3-di-*tert*-butoxy-2-propanol) and
496 TTBG (tri-*tert*-butoxy-propane). Side reactions can occur such as the dehydration of TBA
497 to isobutylene (IB) followed of its dimerization. Under the performed reaction conditions,
498 no diisobutylene is detected (**Figure C1**) and the isobutylene yield estimated from the
499 autogenous pressure is negligible (less than 1%). **Figure 11** compares MTBG (primary
500 product) and the h-GTBG (DTBG and TTBG) molar yields as function of the overall
501 glycerol conversion employing Amberlyst[®] 15 and commercial zeolites as catalysts. **Table**
502 **2** reports conversion and product selectivity obtained after 10 h of reaction.

503 Using A-15, the yield of the primary product reaches a maximum at *ca.* 50%
504 glycerol conversion (**Table 2**). The DTBG (secondary product) is starting to be formed at
505 30% glycerol conversion (extrapolated value at zero conversion). After 10 h of reaction,
506 one quarter of the products are composed of DTBG, whereas the yield of TTBG (ternary
507 product) is negligible (0.3%). Employing the large pores zeolites (*BEA, FAU and MOR)
508 the di-substituted ethers begin to be formed at a much lower glycerol conversion than for
509 A-15, *i.e.* below 6% (**Figure 11**). After 10 h of reaction, the selectivity into DTBG is 5%
510 higher for (BEA)_{NC}^{12,5} than for A-15. (FAU)_{SC}¹⁷, is more selective for the formation of the di-
511 substituted ether than the *BEA zeolite, the small difference provides from a higher yield
512 into 1,2,3-tri-*tert*-butoxy propane. For (MOR)_{NC}¹⁰ the selectivity into DTBG is low (1%),
513 ascribable to the low glycerol conversion (6%). The medium pore zeolite (MFI)_{NC}⁴⁵ is almost
514 totally selective to MTBG (99 %) even for a conversion of 20% (**Table C2**).

515 In comparison with the sulfonic resin (A-15), which is a macroporous solid that
516 hence features no spatial constraint, the use of large pore zeolites favors at low conversions
517 successive etherification reactions ascribable to the overconcentration of ethers in the
518 micropores resulting from steric hindrance. It can thus be assumed that zeolite catalysis
519 induces "product shape selectivity" [16]. Yet, Gonzalez *et al.* claimed that the selectivity
520 towards di- and tri-ethers is correlates with the strength of protonic sites [9]. Nevertheless,
521 the correlation put forward is highly disputable and moreover merely valid for one zeolite
522 (*BEA). Hence, the "product shape selectivity" mechanism through zeolite catalysis is a
523 valuable mean that allows for explaining the observed selectivity.

524 **Regeneration:** The deactivated catalysts were regenerated either by (i) rinsing with
525 ethanol at 373 K under 10 MPa nitrogen pressure by using a Dionex ASE 350 apparatus or
526 (ii) through calcination in air at 823 K for 5 h. As expected, calcination allows to recover
527 the entire activity of zeolite catalyst (**Figure 12**). Furthermore, as far as MOR and *BEA
528 zeolites are concerned, rinsing with ethanol allows to recover greatly the catalytic activities,
529 which are 87 and 93%, respectively. The extracted molecules by ethanol rinsing are
530 glycerol and desired conversion products, MTBG and DTBG (only in the case of *BEA).
531 This confirms what has been put forward by Gonzales *et al.*, who evidenced that the
532 deactivation of *BEA zeolite during glycerol etherification resulted from zeolite
533 micropores blocking with the reagent and products [9]. The retention of reactant and
534 products within the micropores is thus due to steric hindrance [67]. These confined
535 molecules are prone to limit or inhibit the bimolecular reaction. It can thus be assumed that
536 the auto-inhibition is responsible for rapid decrease of the reaction rate (as observed in
537 **Figure 8**). The inhibition effect is strongly pronounced for mono-dimensional pore
538 systems, *e.g.* (MOR)_{NC}¹⁰, where a single molecule confined in the pore mouths already

539 prevents the access to reagents to an important amount of acid sites located within the
540 crystal, leading to a very fast deactivation.

541 Rinsing the deactivated (FAU)_{SC}⁴⁰ with ethanol permits to regenerate only partially
542 catalytic activity (up to 60%), despite of recovering entirely the initial Brønsted acidity.
543 Indeed, no interaction was observed between retained molecules (4.2 wt%) and zeolite –OH
544 groups located in the supercages and in the sodalite cages (**Figure C3**). The loss of activity
545 is thus merely due to a steric blockage of trapped molecules. The presence of the retained
546 molecules within the supercages decreases the available space that is enough to inhibit the
547 bimolecular etherification reaction.

548 In the case of (MFI)_{NC}⁴⁵, the ethanol washing allows to recover 30% of catalytic
549 activity, as almost 5.0wt% of molecules remain retained within the micropores upon
550 rinsing. This observation can readily be attributed to the steric blocking of the pore
551 intersections through retained molecules.

552 Washing with ethanol is more efficient on the zeolite featuring straight channels,
553 such as *BEA and MOR zeolites, compared to zeolites possessing larger cavities than the
554 pore size, *i.e.* the FAU supercage or presenting an intersected channel system, such as MFI,
555 where the formation of large molecules is favored. The results obtained in this section thus
556 clearly support the “product shape selectivity” mechanism suggested for the glycerol
557 etherification over zeolites.

558 **4. Conclusion**

559 For *n*-hexane cracking; a reaction without internal diffusion limitations (gas phase
560 reaction at high temperature, small size of reactant and product molecules, monomolecular
561 mechanism), TOFs observed over various zeolites depend on the confinement of the BAS.

562 Confined BAS (in zeolites) are substantially more active compared to unconfined BAS (in
563 meso- or macroporous materials). The apparent activity depends on the local geometry of
564 the site. Indeed, for *BEA and MFI zeolites that feature the same confining voids (0.69 and
565 0.7 nm, respectively) and thus yield similar turnover rates and selectivity.

566 Contrariwise, in a reaction sensitive to diffusion limitation (liquid phase, low
567 temperature, bimolecular mechanism, large products molecules), such as the glycerol
568 etherification with *tert*-butyl alcohol the zeolite confining void is not sufficient to predict
569 activity, selectivity and stability; the accessibility to the void volume has to be taken into
570 account. As an example, *BEA and MFI zeolites feature the same confining voids but the
571 difference in their access (over 1 Å) is sufficient to generate strong diffusion limitations in
572 the case of the medium pore zeolite. For *BEA (12 MR zeolite) the activity is proportional
573 to the concentration of BAS at the condition that the crystal size is lower than 100 nm
574 (absence of internal diffusion limitations). For zeolites featuring the biggest confining voids
575 (*i.e.* the FAU supercage) successive etherification is favoured, yet product desorption is
576 hampered.

577 For liquid phase reactions catalyzed by zeolite active sites the porous geometry (*i.e.*
578 void volume, interconnection, size) has a crucial effect on confinement and shape
579 selectivity and hence on catalytic key parameters (activity, selectivity and stability).

580

581 **Acknowledgements**

582 C. Miranda thanks Colciencias for the financial support provided for doctoral formation
583 through the 617 convocation. A. Astafan, thanks the Programme PAUSE and the
584 University of Poitiers for their financial supports.

585

586 **References**

587

- 588 [1] M. Pagliaro, R. Ciriminna, H. Kimura, M. Rossi, C. Della Pina, *Angew. Chem.*
589 *Inter. Ed.*, 46 (2007) 4434.
- 590 [2] C. Len, R. Luque, *Sus. Chem. Proc.*, 2 (2014) 1.
- 591 [3] J.F. Izquierdo, M. Montiel, I. Palés, P.R. Outón, M. Galán, L. Jutglar, M.
592 Villarrubia, M. Izquierdo, M.P. Hermo, X. Ariza, *Ren. and Sus. En. Rev.*, 16 (2012)
593 6717.
- 594 [4] M. Sutter, E.D. Silva, N. Duguet, Y. Raoul, E. Métay, M. Lemaire, *Chem. Rev.*, 115
595 (2015) 8609.
- 596 [5] C. Cannilla, G. Bonura, L. Frusteri, F. Frusteri, *Chem. Eng. J.*, 282 (2015) 187.
- 597 [6] E. Theodore, K.R. Edlund, US patent 1968033A (1934) to Shell.
- 598 [7] K. Klepáčová, D. Mravec, M. Bajus, *Appl. Catal. A: Gen.*, 294 (2005) 141.
- 599 [8] K.Y. Nandiwale, S.E. Patil, V.V. Bokade, *En. Tech.*, 2 (2014) 446.
- 600 [9] M.D. González, Y. Cesteros, P. Salagre, *Appl. Catal. A: Gen.*, 450 (2013) 178.
- 601 [10] K. Klepáčová, D. Mravec, A. Kaszonyi, M. Bajus, *Appl. Catal. A: Gen.*, 328 (2007)
602 1.
- 603 [11] D. Mravec, A. Turan, A. Filková, N. Mikesková, E. Volkovicsová, G. Onyestyák, S.
604 Harnos, F. Lónyi, J. Valyon, A. Kaszonyi, *Fuel Proc. Tech.*, 159 (2017) 111.
- 605 [12] M.D. González, P. Salagre, M. Linares, R. García, D. Serrano, Y. Cesteros, *Appl.*
606 *Catal. A: Gen.*, 473 (2014) 75.
- 607 [13] N. Simone, W.A. Carvalho, D. Mandelli, R. Ryoo, *J. Mol. Catal. A: Chem.*, 422
608 (2016) 115.
- 609 [14] P.B. Weisz, V.J. , Frillette, V.J., *J. Phys Chem.*, 64 (1960) 382.

- 610 [15] M. Csicsery, Shape –selective catalysis, chapter 12, p 680-713, in Zeolite chemistry
611 and catalysis, J. A. Rabo, eds ACS **1976**.
- 612 [16] E. G. Derouane, *J. Mol. Cat. A Chem.* 134 (1998) 29.
- 613 [17] K. Okada, T. Tomita, Y. Kameshima, A. Yasumori, K.J.D. MacKenzie, S, *J Coll.*
614 *Inter Sc.*, 219 (1999) 195.
- 615 [18] R.B. Borade, A. Clearfield, *Micro. Mat.*, 5 (1996) 289.
- 616 [19] N. Lauridant, T. Jean Daou, G. Arnold, J. Patarin, D. Faye, *Micro. Meso. Mat.*, 166
617 (2013) 79.
- 618 [20] K. Na, C. Jo, J. Kim, K. Cho, J. Jung, Y. Seo, R.J. Messinger, B.F. Chmelka, R.
619 Ryoo, *Science*, 333 (2011) 328.
- 620 [21] A. Astafan, M.A. Benghalem, Y. Pouilloux, J. Patarin, N. Bats, C. Bouchy, T.J.
621 Daou, L. Pinard, *J. Catal.*, 336 (2016) 1.
- 622 [22] I. Kabalan, I. Khay, H. Nouali, A. Ryzhikov, B. Lebeau, S. Albrecht, S. Rigolet, M.-
623 B. Fadlallah, J. Toufaily, T. Hamieh, J. Patarin, T.J. Daou, *J. Phys. Chem. C*, 119
624 (2015) 18074.
- 625 [23] J.M.D. Coutanceau C., M F Alvarez, M. Guisnet, *J. Chim. Phys. Physico-Chim.*
626 *Biol.*, 94 (1997) 765.
- 627 [24] S.K. Saxena, A.a.H. Al-Muhtaseb, N. Viswanadham, *Fuel*, 159 (2015) 837.
- 628 [25] M. Guisnet, P. Ayrault, J. Datka, , *Pol. J. Chem.*, 71 (1997) 1455.
- 629 [26] M. A. Makarova, K. Karim, J. Dwyer, *Micro. Mat.*, 4 (1995) 243.
- 630 [27] C.A. Emeis, *J. Catal.*, 141 (1993) 347.
- 631 [28] G. Shi, H. Zhang, *J. Quant. Spect. Rad. Tans.*, 105 (2007) 459.

- 632 [29] A. Bauer, M. Godon, J. Carlier, Q. Ma, R. H. Tipping, *J. Quant. Spect. Rad. Tans.*,
633 50 (1993) 463.
- 634 [30] M.T. Tran, N.S. Gnep, G. Szabo, M. Guisnet, *J. Catal.*, 174 (1998) 185.
- 635 [31] V. C. Nguyen, N. Q. Bui, P. Mascunan, T. T. H. Vu, P. Fongarland, N. Essayem,
636 *Appl. Catal. A Gen.*, 552 (2018) 184.
- 637 [32] J.-C. Kim, K. Cho, R. Ryoo, *Appl. Catal. A: Gen.*, 470 (2014) 420.
- 638 [33] K. Kim, R. Ryoo, H.-D. Jang, M. Choi, *J. Catal.*, 288 (2012) 115.
- 639 [34] B. Xu, C. Sievers, S. B. Hong, R. Prins, J. A. van Bokhoven, *J. Catal.*, 244 (2006)
640 163.
- 641 [35] C.V. Mc Daniel, P.K. Maher, *Zeolite chemistry and Catalysis*, ACS Monograph,
642 Washington D.C, 1976, 266.
- 643 [36] P.K. Maher, F.D. Hunter, J. Scherzer, *Molecular sieve Zeolites-1.*, *Adv. Chem. Ser.*,
644 101 (1970) 266.
- 645 [37] R.D. Shannon, K.H. Gardner, R.H. Staley, G. Bergeret, P. Gallezot, A. Auroux, J.
646 *Phys. Chem.*, 89 (1985) 4478.
- 647 [38] W.O. Haag, R.M. Lago, P.B. Weisz, *Nature*, 309 (1984) 589.
- 648 [39] S.M. Babitz, B.A. Williams, J.T. Miller, R.Q. Snurr, W. O. Haag, H.H. Kung, *Appl.*
649 *Catal. A: Gen.*, 179 (1999) 71.
- 650 [40] T.F. Narbeshuber, H. Vinek, J.A. Lercher, *J. Catal.*, 157 (1995) 388.
- 651 [41] C. Mirodatos, D. Barthomeuf, *J. Chem. Soc. Chem. Commun.*, (1981) 39.
- 652 [42] M., Niwa, S. Sota, N. Katada, *Catal. today*, 185 (2012) 17.
- 653 [43] W. O. Haag, R.M. Dessau, R. M. Lago, *Stud. Surf. Sci. Catal.*, 60 (1991) 255.
- 654 [44] S. Li, A. Zheng, Y., Su, H. Zhang, L. Chen, J. Yang, C. Ye, F. Deng, *J. Am. Chem.*
655 *Soc.*, 129 (2007) 11161.

656 [45] R. Gounder, A. J. Jones, R. T. Carr, E. Iglesia, *J. Catal.*, 286 (2012) 214.

657 [46] W. O. Hagg, R. M. Lago, P. B. Weisz, *Faraday Discuss. Chem. Soc.*, 72 (1981) 317.

658 [47] R. Gounder, E. Iglesia, *Chem. Commun.*, 49 (2013) 3491-3509

659 [48] A.J. Jones, R.T. Carr, S. I. Zones, E. Iglesia, *ACS Catal.*, 5 (2015) 5741.

660 [49] M. L. Sarazen, E. Doskocil, E. Iglesia, *J. Catal.*, 344 (2016) 553.

661 [50] W. Kiatkittipong, W. Intaracharoen, P. Laosiripojana, N. Chaisuk, C. Praserthdam,

662 P. Assabumrungrat, *S. Comp. Chem. Eng.*, 35 (2011) 2034.

663 [51] L. Constantinou, R. Gani, *AICHE Journal*, 40 (1994), 1697.

664 [52] P.M. Pico, A. Romero, S. Rodriguez, A. Santos, *Ind. Eng. Chem. Res.*, 51 (2012)

665 9500.

666 [53] R.S. Karinen, A.O.I. Krause, *Appl. Catal. A: Gen.*, 306 (2006) 128.

667 [54] F. Frusteri, F. Arena, G. Bonura, C. Cannilla, I. Sparado, O. Di Blasi, *Appl. Catal.*

668 *A. Gen.*, 367 (2009) 77.

669 [55] S. R. Blaszkowski, R. A. van Santen, *J. Am. Chem. Soc.* 118 (1996) 5152),

670 [56] F. W. Kirsch, J.D. Potts, D.S. Barmby, *J. Catal.* 27 (1972) 142.

671 [57] J. P. van den Berg, J.P. Wolthuizen, A.D.H. Clague, G.R. Hays, R. Huis, J.H.C. van

672 Hoff, *J. Catal.* 80 (1983) 130.

673 [58] P. B. Venuto and P. S. Landis, *Adv. Catal.* 18 (1968) 259,

674 [59] M. Xu, J.H. Lunsford, D.W. Goodman, A. Bhattacharyya, *Appl. Catal. A. Gen.*, 149

675 (1997) 289.

676 [60] F. Yaripour, M. Mollavali, S.M. Jam, H. Atashi, , *Energy Fuels*, 23 (2009) 1896.

677 [61] J.R. Copeland, I.A. Santillan, S.M. Schimming, J.L. Ewbank, C. Sievers, *J. Phys.*

678 *Chem. C*, 117 (2013) 21413.

- 679 [62] M. Guidotti, C. Canaff, J.-M. Coustard, P. Magnoux, M. Guisnet, *J Catal.*, 230
680 (2005) 375.
- 681 [63] P. Magnoux, P. Cartraud, S. Mignard, M. Guisnet. *J. Catal.*, 106 (1987) 235.
- 682 [64] P.M. Veiga, A.C.L. Gomes, C.O. Veloso, C.A. Henriques, *Appl. Catal. A. Gen.*, 548
683 (2017) 2.
- 684 [65] O. Levenspiel, *Chemical reaction engineering*, 3rd Edition Wiley, 1999.
- 685 [66] S. Li, V. A. Tuan, J. L. Falconer, R.D. Noble, *J. Memb. Sci.*, 191 (2001) 53.
- 686 [67] M. Guisnet, P. Magnoux, *Zeolite Microporous Solids: Synthesis*, E Derouane, F.
687 Lemos, C. Naccache, F. R. Ribeiro, F. (Eds.), Springer Netherlands, 1992, p. 457.
- 688 [68] H. Sammoury, J. Toufaily, K. Cherry, T. Hamieh, Y. Pouilloux, L. Pinard, *Appl.*
689 *Catal. A. Gen.*, 551 (2018) 1.

690

691

Table and Figure captions

- 692 **Table 1** Textural and acidic properties of Amberlyst[®] 15, alumina, silica, silica
693 alumina and zeolites (commercial and synthesized): MOR, FAU, *BEA and
694 MFI.
695
- 696 **Table 2** Glycerol etherification with *tert*-butyl alcohol: conversion and selectivity
697 after 10 h, initial activity (A_0) and TOF obtained on Amberlyst[®] 15, silica,
698 alumina, silica-alumina and zeolites (commercial and synthesized): MOR,
699 FAU, *BEA and MFI.
700
- 701 **Fig. 1** Micropore (a) and mesopore (b) volumes and proportion of theoretical
702 Brønsted acid site probed by pyridine at 423 K (c) as a function of zeolite
703 crystal size.
704
- 705 **Fig. 2** Scanning electron microscopy and transmission electronic images of
706 commercial, modified and synthesized zeolites.
707
- 708 **Fig. 3** First-order plot for *n*-hexane cracking over (MFI)_{MC}⁴⁰ at 813 K.
709
- 710 **Fig. 4** Initial activity in *n*-hexane cracking (A_0) as a function of the concentration
711 of protonic site probed by pyridine at 423 K ($[PyH^+]$). (Operating
712 conditions: T = 813 K, P = 1 atm, $P_{N_2}/P_{n-c6} = 9$). The plotted values used

713 with entity “Ref.” correspond to values drawn from Ref [55] and
714 represented in table B2.

715
716 **Fig. 5** TOF as a function of the measure of the diffusion constraint:
717 $L(A_0)^{0.5}$ (Operating conditions: T = 813 K, P = 1 atm, $P_{N_2}/P_{n-c6} = 9$).
718

719
720 **Fig. 6** (a) Conversion normalized by the conversion achieved at 1200 rpm and (b)
721 Selectivity of MTBG and DTBG as function of the stirring rate on
722 $(*BEA)_{NC}^{12.5}$.
723

724 **Fig. 7** Natural logarithm of initial rates ($\ln r_0$) as a function of natural logarithm of
725 the initial concentration ($\ln[X]_0$) of glycerol (full symbols) and TBA (open
726 symbols). Kinetic study carried out on $(*BEA)_{NC}^{12.5}$ at 363 K (data is given as
727 absolute values).
728

729 **Fig. 8** Glycerol conversion as a function of reaction time. Test carried out at 363
730 K, 1200 rpm, autogenous pressure, 7.5% of catalyst (referred to glycerol
731 mass) and glycerol/*tert*-butyl alcohol molar ratio of 0.25.
732

733 **Fig. 9** Initial activity of glycerol etherification with *tert*-butyl alcohol as a function
734 of the concentration of protonic sites probed by pyridine at 423 K.
735 (operating conditions: glycerol/*tert*-butyl alcohol molar ratio = 0.25, T =
736 363 K).
737

738
739 **Fig. 10** Effectiveness factor (η) in etherification of glycerol with *tert*-butyl alcohol
740 as a function of the zeolite beta crystal size (operating conditions:
741 glycerol/*tert*-butyl alcohol molar ratio = 0.25, T = 363 K).
742

743 **Fig. 11** Molar yields of MTBG, DTBG and TTBG as a function of glycerol
744 conversion; Test carried out at 363 K, 1200 rpm, autogenous pressure, 7.5%
745 of catalyst (referred to glycerol mass) and glycerol/*tert*-butyl alcohol molar
746 ratio of 0.25.
747

748 **Fig. 12** Recovered activity after washing with ethanol and calcination of the
749 deactivated catalysts.
750

Supporting information

Section A: generalities

754 **Table A1** Catalyst suppliers.

755	Table A2	Molar composition of the starting synthesis gels and thermal conditions for
756		the preparation of micron-sized (MC), submicron-sized (SC), and
757		nanometer-sized (NC) crystals and nanosponge (NSp)*BEA-type zeolites.
758	Figure A1	Molar extinction coefficient of Brønsted acid site (band at 1545 cm ⁻¹) and
759		Lewis acid site (1455 cm ⁻¹).
760	Figure A2	XRD patterns of the *BEA zeolites and MFI synthesized.
761	Figure A3	Correlation between EFAL and the Lewis acidity.
762		
763	Section B: <i>n</i>-hexane cracking	
764	Figure B1	<i>n</i> -hexane cracking on different catalysts series: FAU, *BEA and MFI. Initial
765		yields into cracking products as a function of initial <i>n</i> -hexane conversion.
766		Operating conditions: T = 813 K, P = 1 atm, P _{N2} /P _{n-c6} = 9
767	Figure B2	C ₄ /C ₂ and C ₅ /C ₁ molar ratios as a function of initial conversion of <i>n</i> -hexane
768		cracking on different catalysts series: FAU, *BEA and MFI. Operating
769		conditions: T = 813 K, P = 1 atm, P _{N2} /P _{n-c6} = 9.
770	Figure B3	<i>n</i> - hexane conversion as a function of time of stream (TOS). Operating
771		conditions: T = 813 K, P = 1 atm, P _{N2} /P _{n-c6} = 9.
772	Table B1	Initial activity in <i>n</i> -hexane cracking obtained on Amberlyst [®] 15, and zeolites
773		(commercial, modified and synthesized): MOR, FAU, *BEA and MFI.
774		Operating conditions: T = 813 K, P = 1 atm, P _{N2} /P _{n-c6} = 9
775	Table B2	Reference catalysts used in the laboratory drawn from [64].
776		
777		
778		
779		
780	Section C: etherification of glycerol with <i>tert</i>-butyl alcohol	
781	C.M.1.	Method for calculation of the effectiveness factor from two crystal sizes and
782		two catalyst activities.

783 **Figure C1** Typical chromatogram for the etherification of glycerol with *tert*-butyl
784 alcohol.

785 **Figure C2** Glycerol conversion as a function of reaction time at 363 K, 1200 rpm,
786 autogenous pressure, 7.5% of catalyst and glycerol/*tert*-butyl alcohol molar
787 ratio of 0.25.

788 **Figure C3** FT-IR spectra of (FAU)₄₀⁴⁰ : fresh and spent catalyst after rinsing with ethanol

789 **Table C1** Thermodynamic data.

790 **Table C2** Selectivity into glycerol monoethers (MTBG), glycerol diethers (DTBG) and
791 glycerol triether (TTBG) at isoconversion. ($X \approx 20\%$) obtained on MOR,
792 FAU, *BEA and MFI catalysts.

Table 1. Textural and acidic properties of Amberlyst® 15, alumina, silica, alumina-silica and zeolites (commercial and synthesized): MOR, FAU, *BEA and MFI.

	Catalyst	Origin ^a	Si/Al		EFAL ^d Atom per cell	Crystal size ^e (L) nm	V _{micro} ^f cm ³ g ⁻¹	V _{meso} ^g cm ³ g ⁻¹	[PyH ⁺] ^h μmol g ⁻¹	[PyL] ⁱ μmol g ⁻¹
			Bulk ^b	Fram. ^c						
MOR	A-15	C	/			/	/	2370	/	
	SiO ₂							0	0	
	Al ₂ O ₃	S	/					0	321	
	SiO ₂ -Al ₂ O ₃	S [17]	20				0.03	1.00	103	96
	(MOR) _{SC} ¹⁰	C	10	11.6	0.6	500-100	0.20	0.06	1056	31
FAU	(FAU) _{SC} ^{2,6}	C	2.6	3.9	19.6	1000-600	0.34	0.07	403	149
	(FAU) _{SC} ¹⁷	C	17	16	0.4	500	0.32	0.15	197	44
	(FAU) _{SC} ⁴⁰	C	40				0.29	0.20	100	20
*BEA	(*BEA) _{MC} ¹⁵	S [18]	15	17	0.5	10000-6000	0.22	0.02	752	215
	(*BEA) _{SC} ⁹	S [18]	9	17	3.1	1500-300	0.25	0.12	470	490
	(*BEA) _{SC} ¹⁰	S [18]	10	13	1.4	700-100	0.25	0.29	798	186
	(*BEA) _{NC} ^{12,5}	C	12	15	1.0	20	0.22	0.58	487	352
	(*BEA) _{NC} ¹⁵	S [19]	15	23 (21)	1.4	40	0.24	0.71	354	336
	(*BEA) _{NSp} ¹⁷	S[20, 21]	17	22 (23)	0.8	2-4	0.24	0.74	130	176
MFI	(MFI) _{MC} ⁴⁰	C	40			250	0.17	0.07	304	44
	(MFI) _{NC} ⁴⁵	C	45			20-50	0.18	0.36	332	25
	(MFI) _{NSh} ⁴⁵	S[22]	45			2	0.18	0.36	83	119
	(MFI) _{NSp} ²⁰	S[22]	20			3.7-4.6	0.17	0.98	151	44

a. C: commercial, S: synthesized, M: modified b. XRF analysis; c. estimated to TOT band at 1080-1200 cm⁻¹ using the correlation given in ref [23-24] or by ²⁷Al and ²⁹Si NMR (in parenthesis), d. Extra-framework Aluminum calculated from b and c. e. according to TEM and SEM images (Fig. 2)., f, g. micropore volume using *t*-plot method; mesopore volume = V_{total} - V_{micro} (V_{total}: determined from the adsorbed volume at p/p₀=0.9), total microporous volume estimated by DR method, h, i. Concentrations of Brønsted ([PyH⁺]) and Lewis ([PyL]) sites able to retain pyridine at 423 K

Table 2. Glycerol etherification with *tert*-butyl alcohol: conversion and selectivity after 10 h, initial activity (A_0) and TOF obtained on Amberlyst[®] 15, silica, alumina, silica-alumina and zeolites (commercial and synthesized): MOR, FAU, *BEA and MFI.

Catalyst	Conv. (%)	Selectivity (%)		$A_{0\text{glycerol}}$ (mol h ⁻¹ g ⁻¹) x 10 ⁴	TOF ^a (h ⁻¹) x 10 ²
		MTBG	h-GTBE		
A-15	64	75	25 (0.3)	15.00	63
SiO ₂	0	0	0	0	0
Al ₂ O ₃	0	0	0	0	0
SiO ₂ -Al ₂ O ₃	2	100	0	0.22	51
(MOR) _{NC} ¹⁰	9	97	3	0.57	5
(FAU) _{SC} ^{2,6}	5	100	0	1.33	33
(FAU) _{SC} ¹⁷	33	82	18 (0.6)	3.26	166
(FAU) _{SC} ⁴⁰	23	83	17 (0.6)	1.36	136
(*BEA) _{MC} ¹⁵	12	93	7	0.08	1
(*BEA) _{SC} ⁹	61	74	26	9.90	198
(*BEA) _{SC} ¹⁰	57	81	19	5.60	70
(*BEA) _{NC} ^{12,5}	54	70	30 (0.1)	7.00	151
(*BEA) _{NC} ¹⁵	57	71	29 (0.1)	4.80	161
(*BEA) _{NSp} ¹⁷	8	92	8	1.90	180
(MFI) _{MC} ⁴⁰	8	99	< 1	0.31	10
(MFI) _{NC} ⁴⁵	20	99	< 1	0.89	41
(MFI) _{NSh} ⁴⁵	12	99	< 1	0.13	46
(MFI) _{NSp} ²⁰	6	99	< 1	0.47	9

Reaction conditions: 7.5 wt.% of catalyst (referred to glycerol mass), glycerol/*tert*-butyl alcohol molar ratio = 0.25, reaction temperature = 363 K, reaction time = 10 h, stirring = 1200 rpm. MTBG: glycerol monoethers; h-GTBE: glycerol diethers + glycerol triether. In parenthesis, selectivity to glycerol triether (%). ^a Turnover frequency per Brønsted acid sites probed by the pyridine at 423 K,

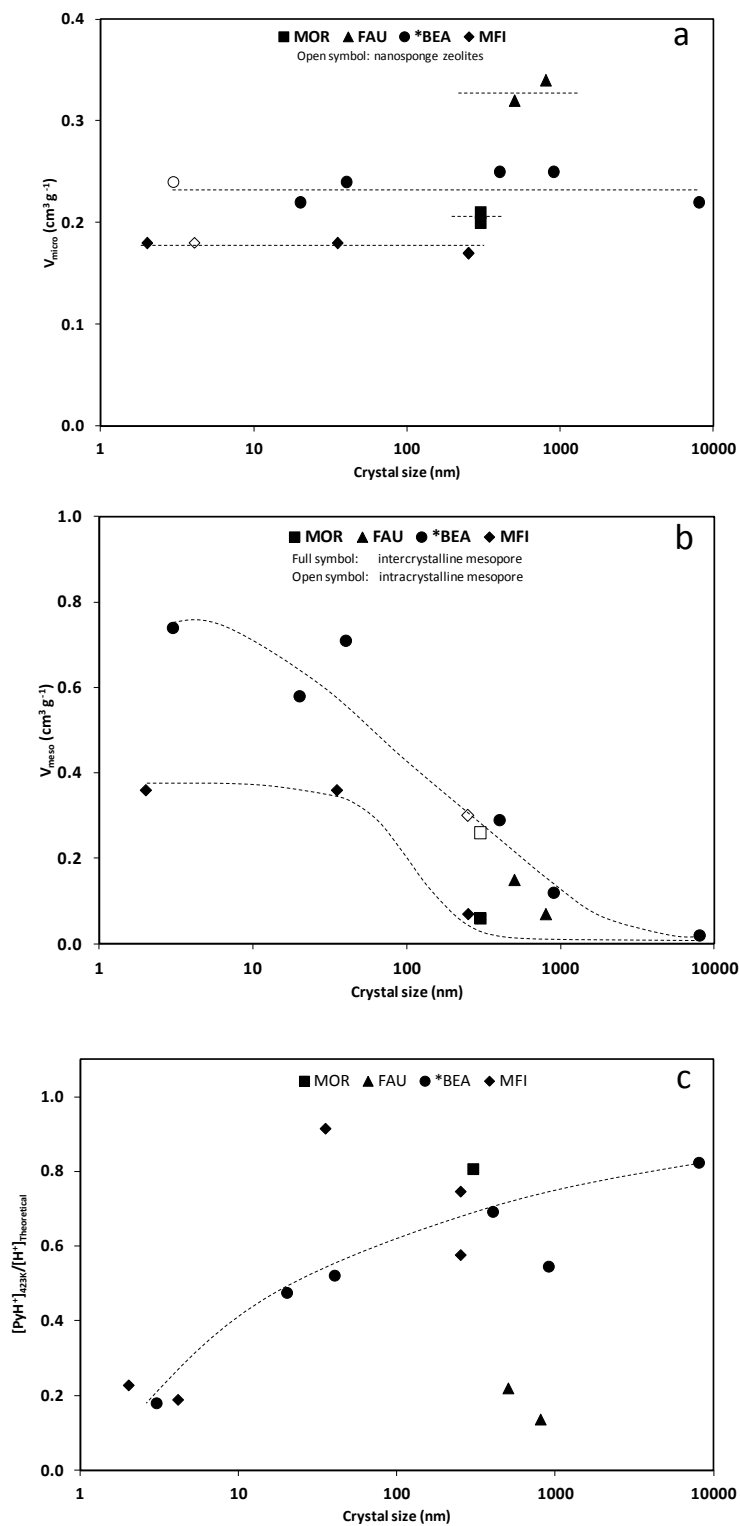


Figure 1. Micropore (a) and mesopore (b) volumes and proportion of theoretical Brønsted acid site probed by pyridine at 423 K (c) as a function of zeolite crystal size.

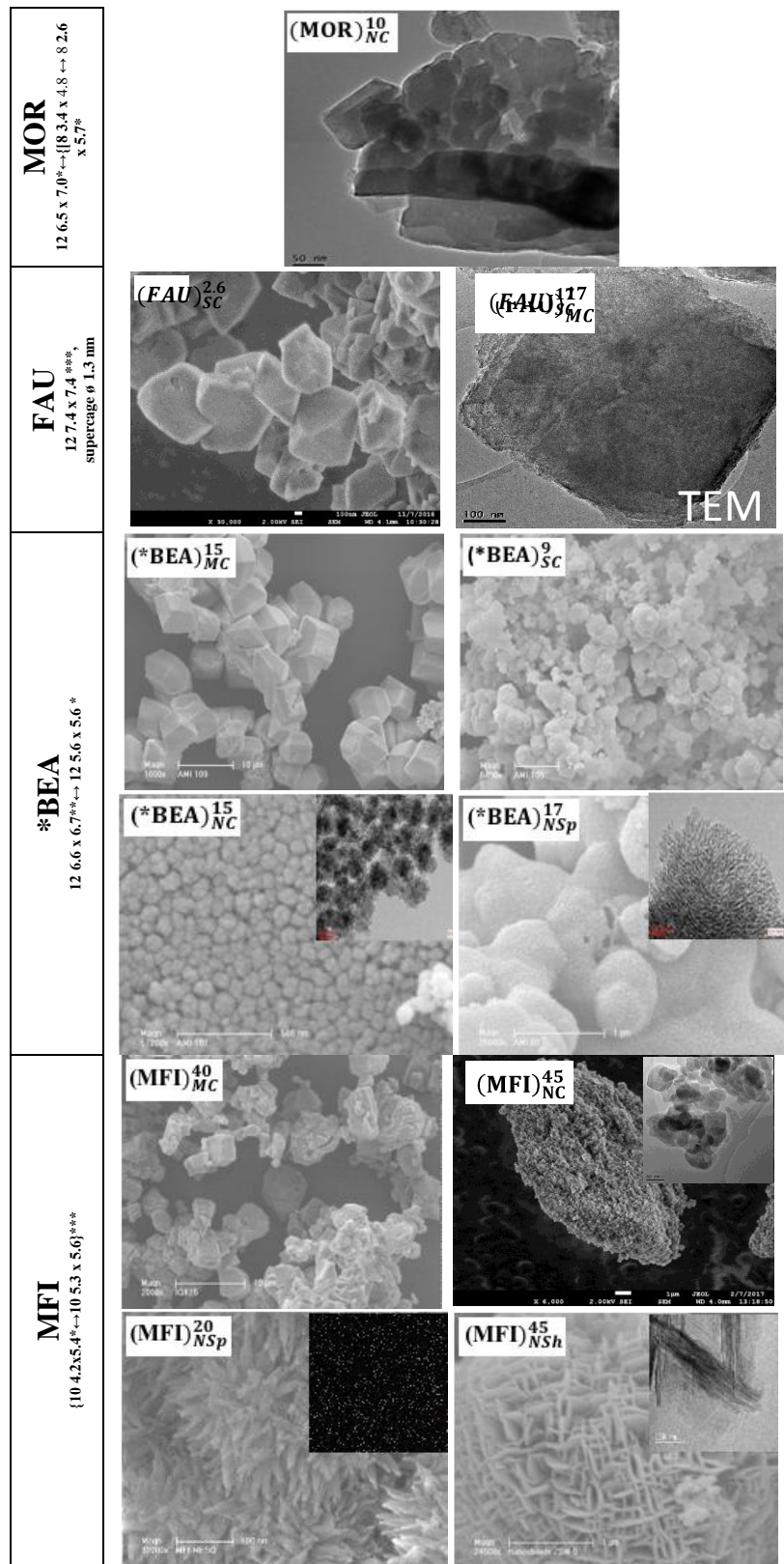


Figure 2. Scanning electron microscopy and transmission electronic images of commercial, modified and synthesized zeolites.

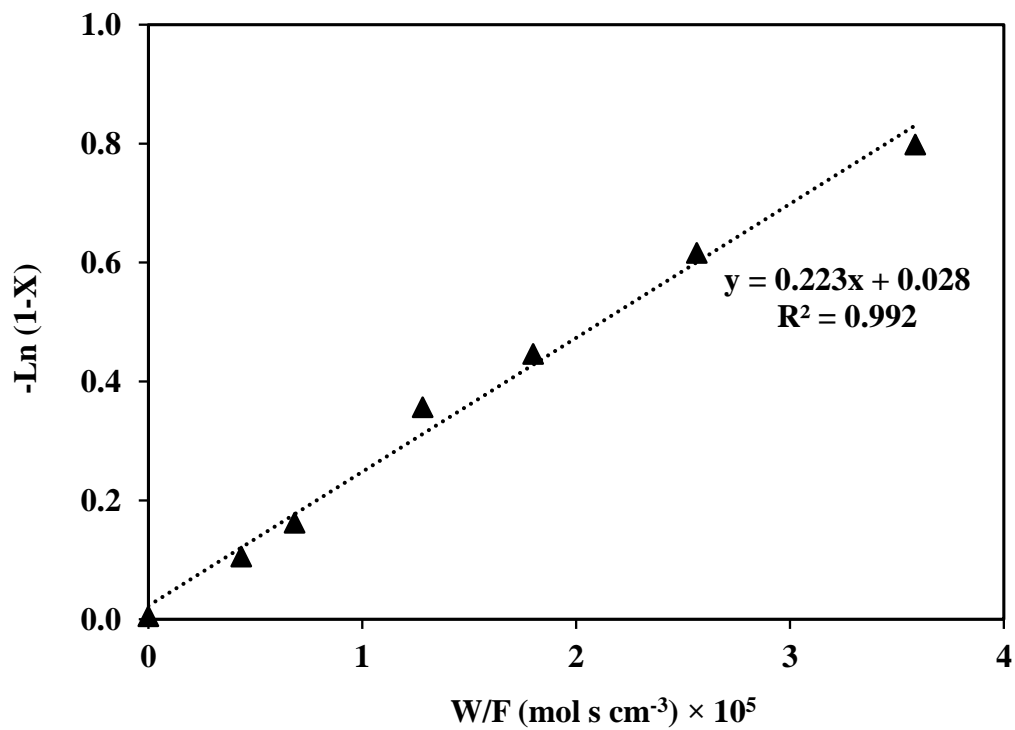


Figure 3. First-order plot for *n*-hexane cracking over (MFI)_{MC}⁴⁰ at 813 K.

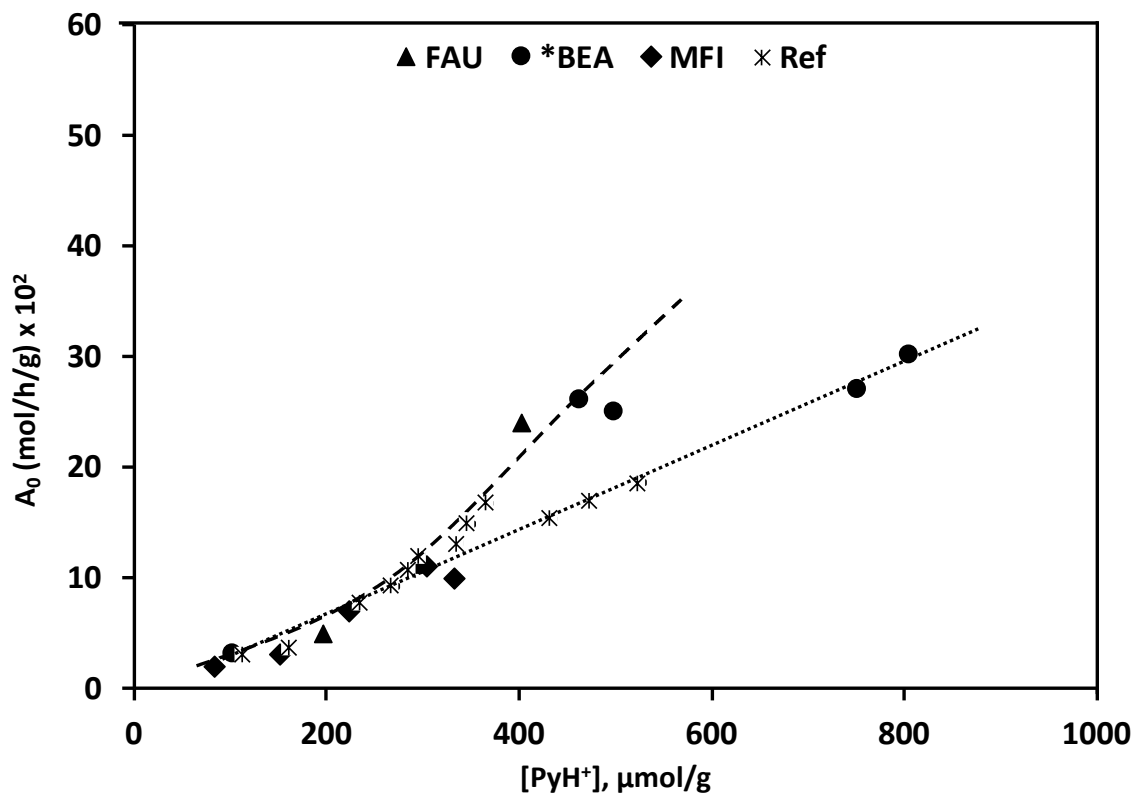


Figure 4. Initial activity in *n*-hexane cracking (A_0) as a function of the concentration of protonic site probed by pyridine at 423 K ($[\text{PyH}^+]$). (Operating conditions: $T = 813$ K, $P = 1$ atm, $P_{\text{N}_2}/P_{\text{n-c}_6} = 9$). The plotted values used with entity “Ref.” correspond to values drawn from Ref [68] and represented in **table B2**.

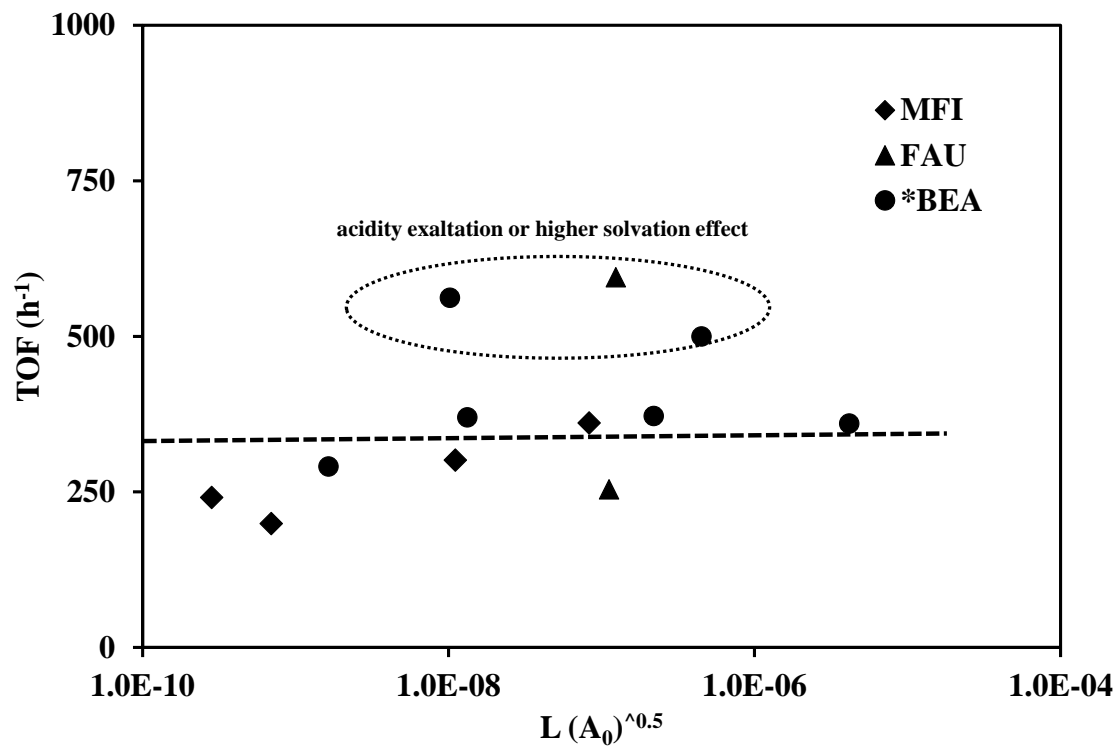


Figure 5. TOF as a function of the measure of the diffusion constraint: $L(A_0)^{0.5}$. (Operating conditions: $T = 813$ K, $P = 1$ atm, $P_{N_2}/P_{n-c6} = 9$).

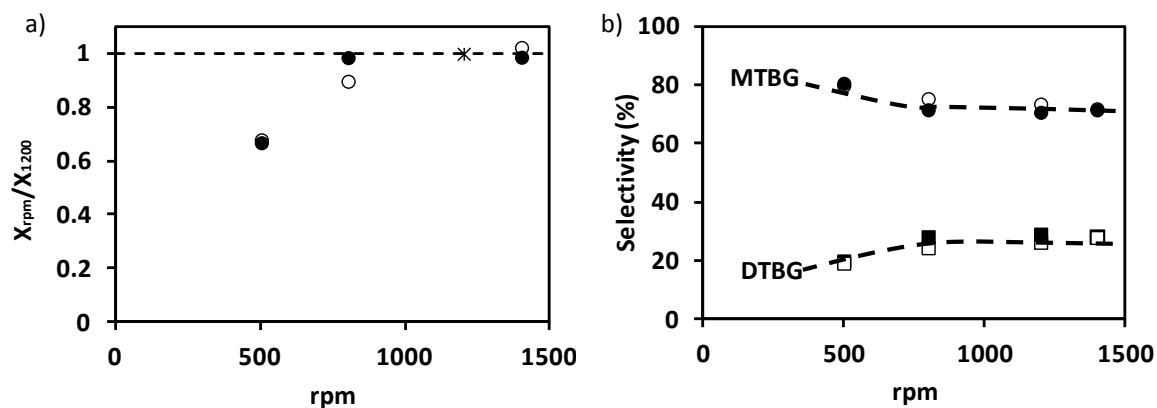


Figure 6. (a) Conversion normalized by the conversion achieved at 1200 rpm and (b) Selectivity of MTBG and DTBG as function of the stirring rate on $(*BEA)_{NC}^{12.5}$.

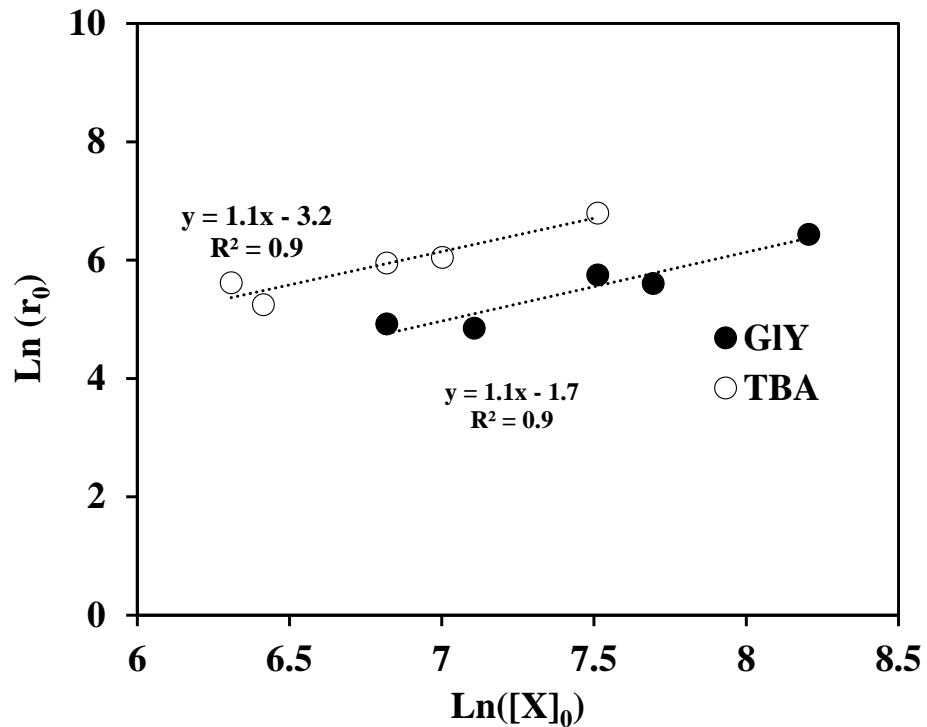


Figure 7. Natural logarithm of initial rates ($\ln r_0$) as a function of natural logarithm of the initial concentration ($\ln[X]_0$) of glycerol (full symbols) and TBA (open symbols). Kinetic study carried out on $(*BEA)_{NC}^{12.5}$ at 363 K (data is given as absolute values).

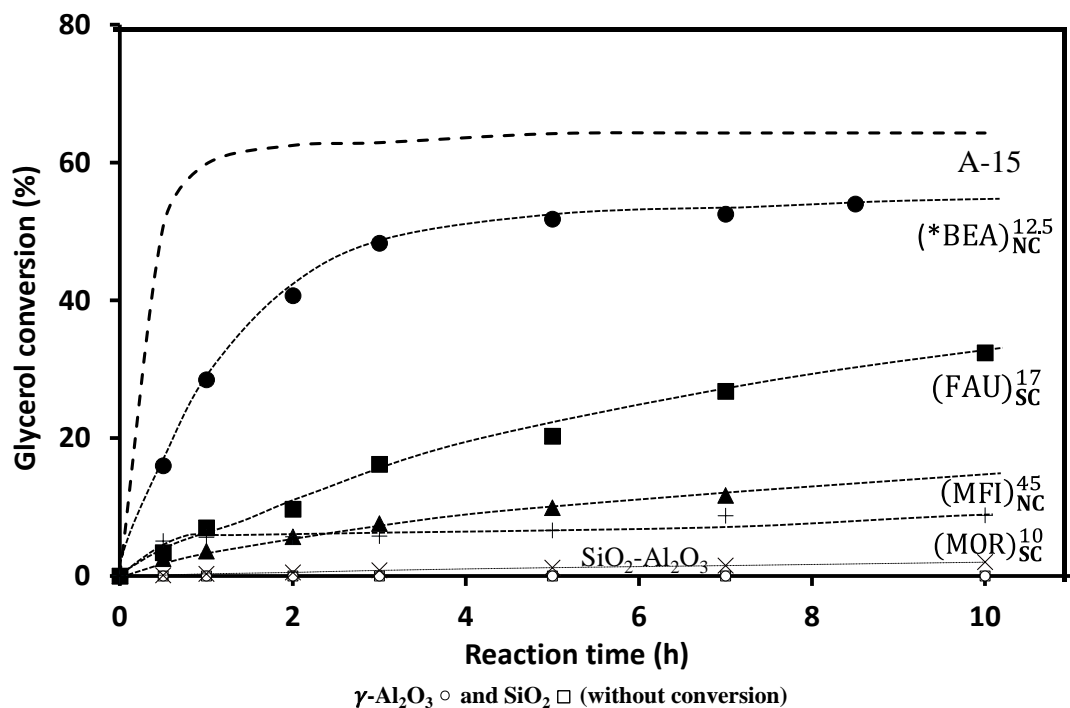


Figure 8. Glycerol conversion as a function of reaction time. Test carried out at 363 K, 1200 rpm, autogenous pressure, 7.5% of catalyst (referred to glycerol mass) and glycerol/*tert*-butyl alcohol molar ratio of 0.25.

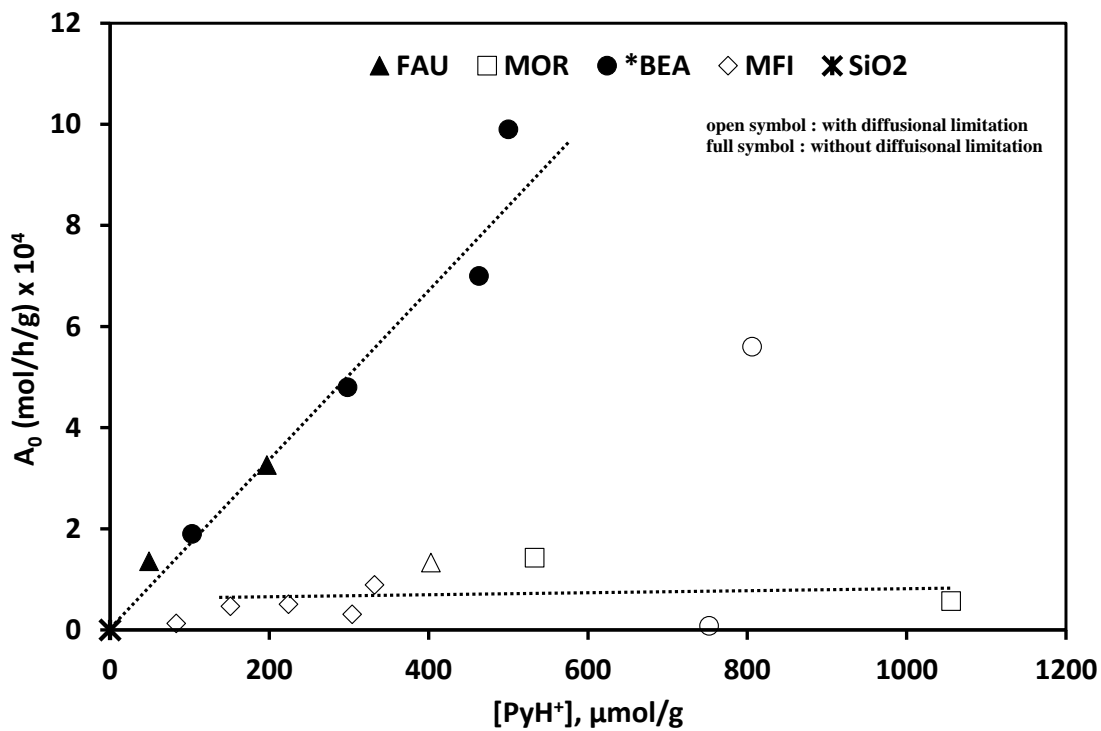


Figure 9. Initial activity of glycerol etherification with *tert*-butyl alcohol as a function of the concentration of protonic sites probed by pyridine at 423 K. (operating conditions: glycerol/*tert*-butyl alcohol molar ratio = 0.25, T = 363 K).

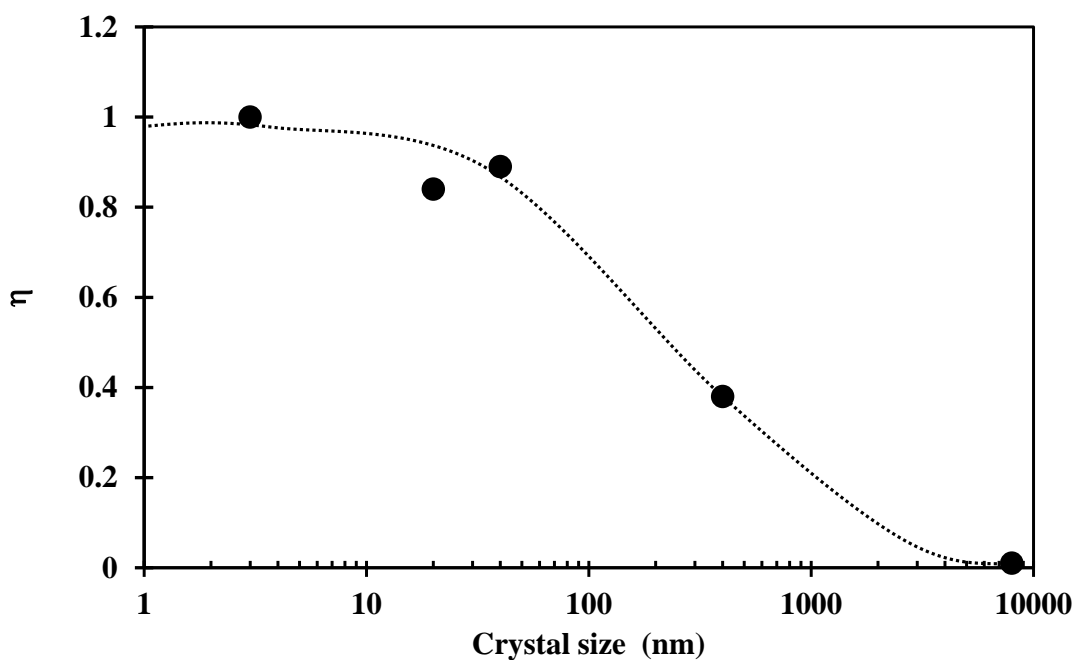


Figure 10. Effectiveness factor (η) in etherification of glycerol with *tert*-butyl alcohol as a function of the zeolite beta crystal size (operating conditions: glycerol/*tert*-butyl alcohol molar ratio = 0.25, $T = 363$ K).

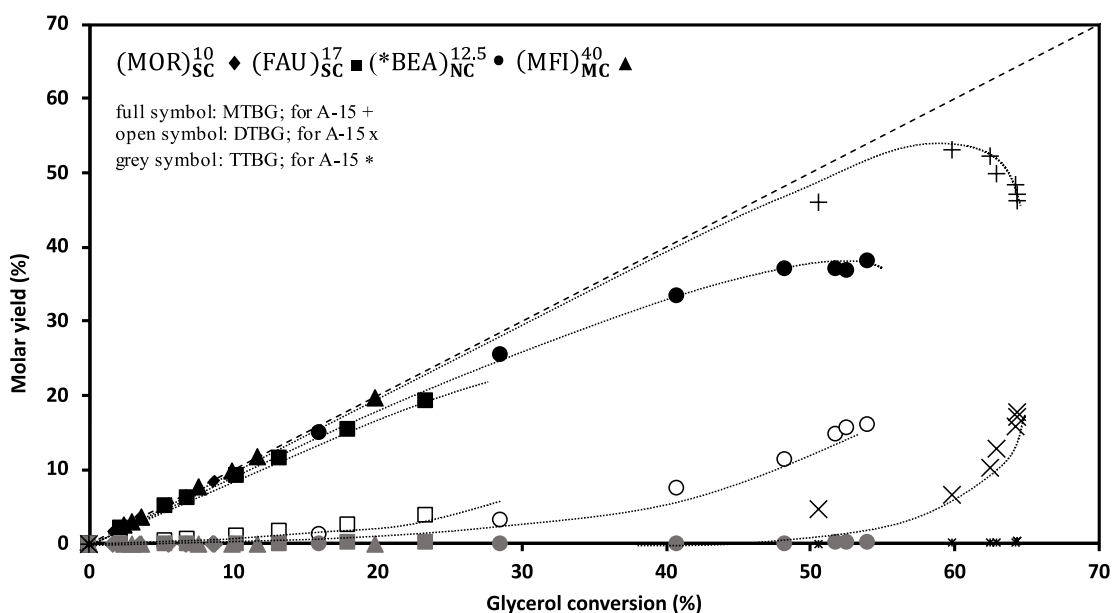


Figure 11. Molar yields into MTBG, DTBG and TTBG as a function of glycerol conversion. Test carried out at 363 K, 1200 rpm, autogenous pressure, 7.5 % of catalyst (referred to glycerol mass) and glycerol/*tert*-butyl alcohol molar ratio of 0.25.

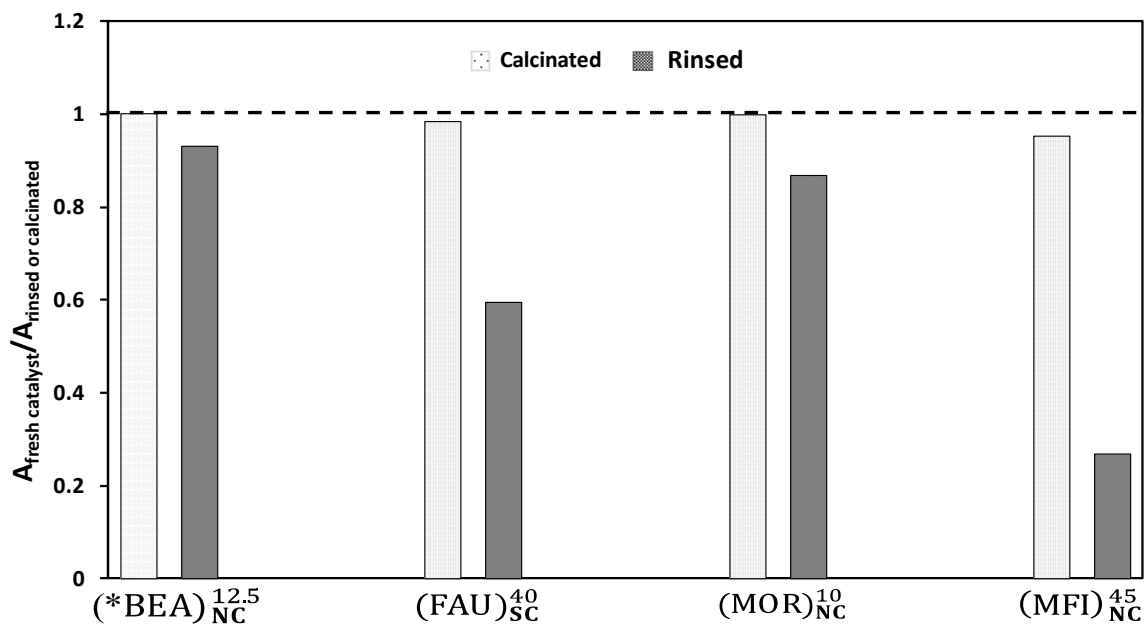


Figure 12. Recovered activity after washing with ethanol and calcination (550 °C/6 h) of the deactivated catalysts.

Supporting information

Section A: generalities

Section B: *n*-hexane cracking

Section C: etherification of glycerol with *tert*-butyl alcohol

Section A: generalities

Table A1. Catalyst suppliers

Catalyst	Supplier	Reference
A-15	Acros Organics	9037-24-5
SiO ₂	Sigma-Aldrich	242179
(MOR) _{SC} ¹⁰	Sud-chemie (Clariant)	T-4545
(FAU) _{SC} ^{2.6}	Zeolyst	CBV500
(FAU) _{SC} ¹⁷	Zeolyst	CBV720
(FAU) _{SC} ⁴⁰	Zeolyst	CBV780
(*BEA) _{NC} ^{12.5}	PQ Zeolites B.V.	CP811 BL-25
(MFI) _{MC} ⁴⁰	Zeolyst	CBV8014
(MFI) _{NC} ⁴⁵	Clariant	HCZP90

A.1. Catalyst synthesis protocol

Synthesis of Silica-alumina [17]

Aluminosilicate was prepared by co-precipitation. Aluminium nitrate nonahydrate (Al(NO₃)₃·9H₂O) and tetraethylorthosilicate (TEOS, Sigma-Aldrich) were used as the starting materials. 18 g of Al(NO₃)₃·9H₂O were first dissolved in absolute ethanol, then 0.5 g of TEOS were added and stirred vigorously for 3 h. After the solution was stirred, 25 wt% NH₄OH aqueous solution (100 ml) was added rapidly with vigorous stirring to obtain a precipitate. The precipitates were immediately dried using an evaporator at 333 K for 2 h, then at 373 K for 15 h in an oven. The resultant solid was calcined at 573 K for 4 h to obtain the aluminosilicate.

Synthesis of γ -Al₂O₃

γ -Al₂O₃ was prepared from aluminium nitrate nonahydrate (Al(NO₃)₃·9H₂O). 7.36 g of Al(NO₃)₃·9H₂O were dissolved in 50 mL deionized water with continuous stirring at 333 K for 2 h. When the solution was heated to 373 K and 13.6 mL of ammonia solution (28%) was added dropwise. After the addition of the ammonia solution was completed stirring continued for a further 12 h at 303 K. The precipitate obtained was filtered, washed with distilled water, and dried at 393 K for 12 h. The solid was calcined at 823 K for 5 h.

Synthesis of *BEA-type zeolite micron-sized crystal [18]

The synthesis mixture was prepared by hydrolyzing tetraethylorthosilicate (TEOS) (98 wt%, Aldrich) in an aqueous solution of tetraethylammonium hydroxide (TEAOH) (35 wt% in aqueous solution, Aldrich). Then a solution made by dissolving metal aluminum (99.95%, Aldrich) in aqueous TEAOH was added and the mixture was kept under stirring until the complete evaporation of ethanol formed upon hydrolysis of TEOS. Finally, hydrofluoric acid (40 wt% in H₂O) was added. The obtained gel (composition in the **Table A2**), was hydrothermally treated at 443 K for 14 days in a Teflon lined stainless steel autoclave. After the required crystallization time, the autoclave was cooled down to room temperature. The pH of the mother liquor was in the range 8–9.5. The product was filtered and washed extensively with distilled water. Finally, the sample was calcined under air at 823 K during 5 h with a temperature ramp of 274 K per minute in order to remove the organic template.

Synthesis of *BEA-type zeolite submicron-sized crystal [18]

For the synthesis of the sub-micron-sized (SC) * BEA-type zeolite, aluminum (Al, Fluka, 99%) was mixed with tetraethylammonium hydroxide solution (TEAOH, Aldrich, 35 wt. %

in H₂O) at room temperature. After, tetraethylorthosilicate (TEOS, Aldrich, 98%) was added to the initial solution and mixed until the complete evaporation of water and ethanol. To the dry gel obtained, water and hydrofluoric acid (HF, Aldrich, 40 wt. % in H₂O) were added and mixed during 4 h to room temperature. The resulting white gel (**Table A2**) were transferred to an autoclave to 443 K during 14 days. Finally, the solid was filtered and washed with water, dried at 373 K during 12 h and calcined to 823 K during 5 h.

Synthesis of *BEA-type zeolite nanometer-sized crystal [19]

A precursor solution of molecular composition 0.014 Na₂O–0.18 (TEA)₂O–0.020 Al₂O₃–1 SiO₂–11.80 H₂O was hydrothermally treated at 368 K for 9 days in a polypropylene bottle. The chemical reagents used were aluminum isopropoxide (98 wt%, Aldrich), tetraethylammonium hydroxide (TEAOH, 35 wt% in aqueous solution, Aldrich), sodium hydroxide (99.99 wt%, Riedel de Haën) and silica powder resulting from the lyophilization of colloidal silica (Ludox AS-40, Aldrich). The resulting milky solution of *BEA zeolite was purified by several centrifugation–dispersion cycles in distilled water (at 20 000 rpm for 30 min). In order to remove the template occluded in the porosity (tetraethylammonium), the final sample was calcined under air at 823 K during 5 h with a temperature ramp of 274 K per minute.

Synthesis of *BEA-type zeolite nano-sponge [20-21]

The NS sample was synthesized using a poly-quaternary ammonium surfactant denoted by N₄-phe.. In a typical synthesis of *BEA nanosponge, ethanol (99.9%), sodium hydroxide (99.99 wt%, Riedel de Haën), sodium aluminate (56.7 wt% Al₂O₃, 39.5 wt% Na₂O) and TEOS (98 wt%, Aldrich) were mixed to obtain a gel composition of 0.22 Na₂O–0.05 N₄-phe–0.025 Al₂O₃–1 SiO₂–4 (ET)₂O–71 H₂O. The resulting gel mixture was maintained under magnetic stirring at 333 K for 6 h. The final gel was transferred to a Teflon-lined

stainless-steel autoclave and heated at 413 K for 4 days under tumbling conditions at 60 rpm. After crystallization, the zeolite product was filtered, washed with distilled water and dried at 393 K. The products were calcined at 873 K for 4 h under air in order to remove the organic surfactant. The protonated form of MC, NC and NS zeolites was obtained by double ion exchange of the calcined zeolite with a 1 M NH_4NO_3 solution (liquid/solid ratio: 20 mL/g) at 353 K for 1 h and calcination in a static oven at 823 K for 5 h.

Table A2. Molar composition of the starting synthesis gels and thermal conditions for the preparation of micron-sized (MC), submicron-sized (SC), and nanometer-sized (NC) crystals and nanosponge (NSp)*BEA-type zeolites.

Reagents	Catalyst	(*BEA) _{MC} ¹⁵	(*BEA) _{SC} ⁹	(*BEA) _{SC} ¹⁰	(*BEA) _{NC} ¹⁵	(*BEA) _{NSp} ¹⁷
	Si	TEOS ^d	TEOS ^d	Aerosil 130	SiO ₂ ^a	TEOS ^d
	Al	Al _(s)	Al _(s)	NaAlO ₂	Al(O-iPr) ₃	NaAlO ₂
Gel composition in molar ratio	HF	0.573	0.680	--	--	--
	Na ₂ O	--	--	0.020	0.014	0.220
	(TEA) ₂ O ^b	0.226	0.340	0.140	0.180	--
	N _{4-phe} ^c	--	--	--	--	0.050
	Al ₂ O ₃	0.016	0.070	0.016	0.020	0.025
	SiO ₂	1	1	1	1	1
	(Et) ₂ O	--	--	--	--	4.00
	H ₂ O	7.03	7.14	15.75	11.80	71.00
Temp.	(K)	443	443	423	368	413
Time	(days)	14	14	16	9	4
Ref.		[18]	[18]	[18]	[19]	[20-21]

^aLudox AS(40) 40% in water lyophilized for 5 days. ^bTEA: (CH₃-CH₂)N-. ^cN_{4-phe}: C₂₂H₄₅N⁺(CH₃)₂-C₆H₁₂-N⁺(CH₃)₂-C₆H₁₃]Br₂. ^dTEOS: Si(OCH₂CH₃)₄; Et: CH₃-CH₂-OH.

Synthesis of (MFI)_{NSh}⁴⁵ catalyst [22]

The diquatery ammonium-type surfactant used for the synthesis of MFI-type nanosheets, has as formula ([C₂₂H₄₅-N⁺(CH₃)₂-C₆H₁₂-N⁺(CH₃)₂-C₆H₁₃]Br₂). Initially, 0.24 g of sodium hydroxide (Riedel de Haen, 99%) was dissolved, at room temperature, in 7.17 g of distilled water in a 45 mL Teflon-lined stainless steel autoclave. Subsequently, 0.73 g of

diquat-C₆-C₂₂ and 0.18 g of sulfuric acid (Aldrich) were then added. After homogenization, 2.13 g of TEOS was added, and a white gel with the following molar composition, 1 SiO₂: 0.3 Na₂O: 0.1 diquat-C₆-C₂₂: 0.18 H₂SO₄: 40 H₂O, was then obtained. The gel was stirred at 1000 rpm during 4 h at 333 K. Then, the mixture was heated at 383 K for 10 days under rotation (30 rpm). After synthesis, the product was recovered by filtration, washed with distilled water, and dried overnight at 373 K. The surfactant was finally removed by calcination in a muffle furnace at 823 K during 8 h in air.

Synthesis of (MFI)_{Nsp}²⁰ catalyst [22]

MFI zeolite with nanosponge morphology was synthesized by using C₁₈H₃₇-N⁺(CH₃)₂-C₆H₁₂-N⁺(CH₃)₂-C₆H₁₂-N⁺(CH₃)₂-C₁₈H₃₇(Br⁻)₃ named C₁₈₋₆₋₆C₁₈ as organic structure-directing agent. Sodium hydroxide (Riedel de Haen, 99%), sodium aluminate (56.7 wt % Al₂O₃, 39.5 wt % Na₂O), tetraethoxysilane (TEOS, Aldrich, 98%) and ethanol (99%) were dissolved in deionized water in a 45 mL Teflon-lined stainless steel autoclave. After homogenization, C₁₈₋₆₋₆C₁₈ was added to set the molar composition of the gel to 100SiO₂:22Na₂O: 2.5Al₂O₃:5C₁₈₋₆₋₆C₁₈:800ETOH:7100H₂O. The gel was stirred at 1000 rpm for 6 h at 333 K, and then placed in a tumbling oven (30 rpm) at 413 K for 4 days. After synthesis, the product was recovered by filtration, washed with deionized water and dried overnight at 393 K. The C₁₈₋₆₋₆C₁₈ surfactant was removed by calcination at 823 K during 4 h in air.

The calibration curves were obtained by adding to the IR cell a known amount of pyridine vapor from a gas admission compartment (0.9122 cm^3). The spectrum were recorded at 293 K.

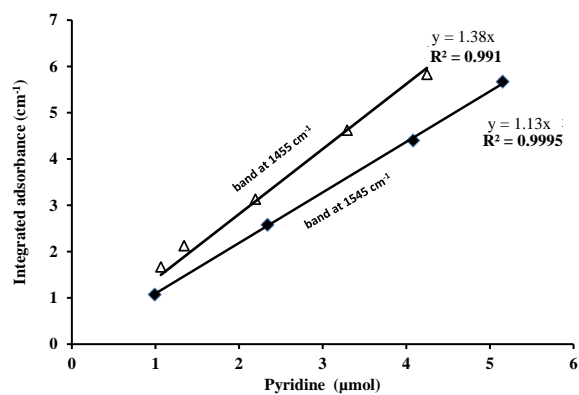


Figure A1. Molar extinction coefficient of Brønsted acid sites (band at 1545 cm^{-1}) and Lewis acid sites (1455 cm^{-1}).

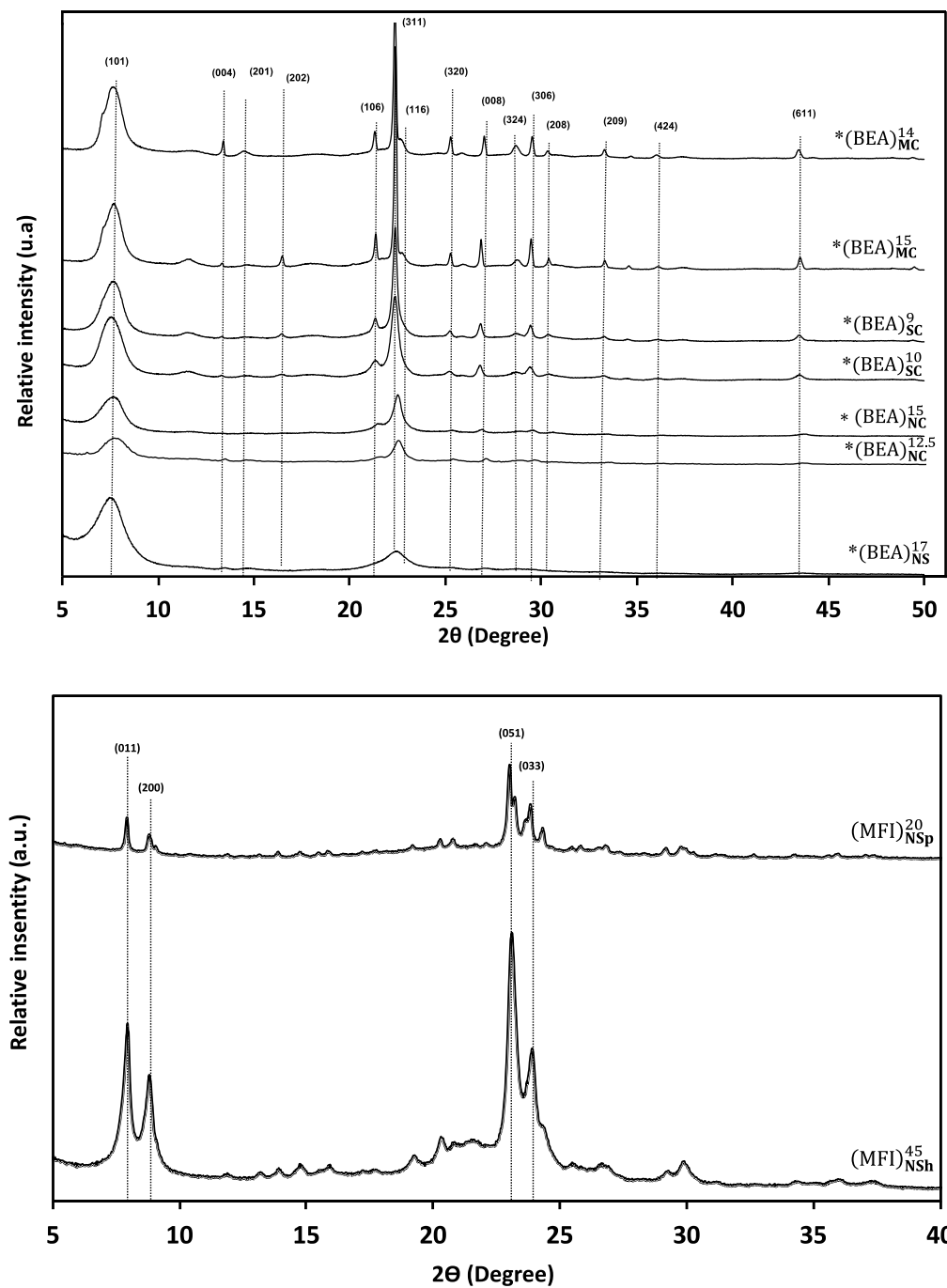


Figure A2. XRD patterns of the *BEA zeolites and MFI synthesized.

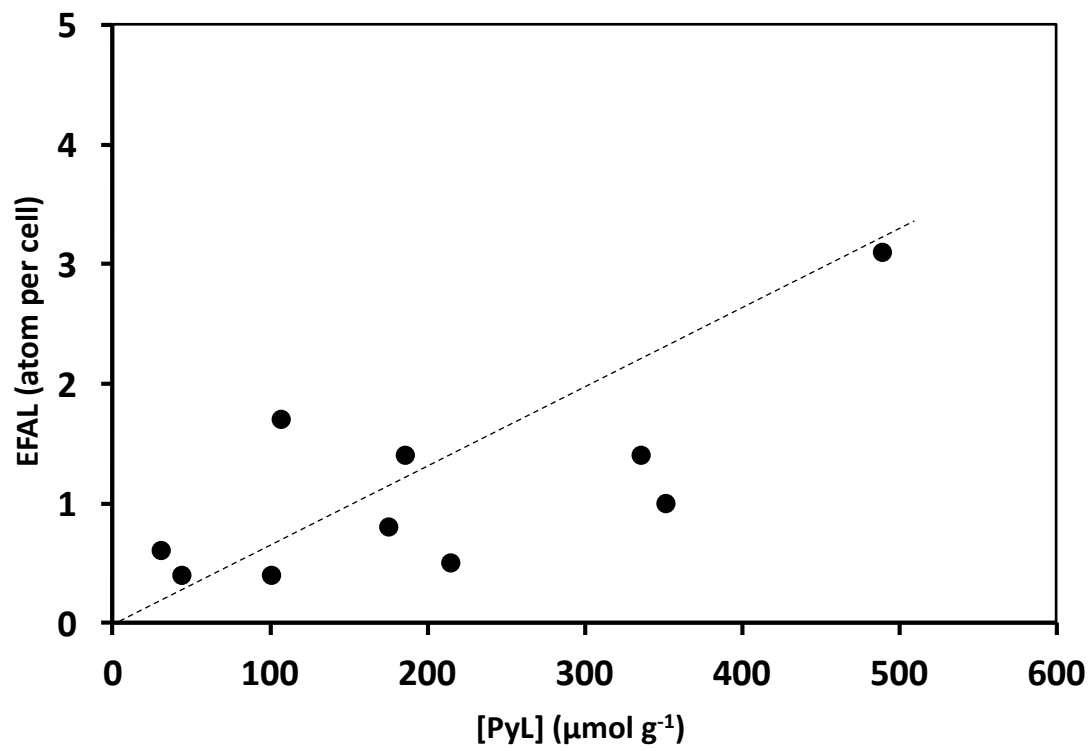


Figure A3. Correlation between EFAL and the Lewis acidity.

Section B: *n*-hexane cracking

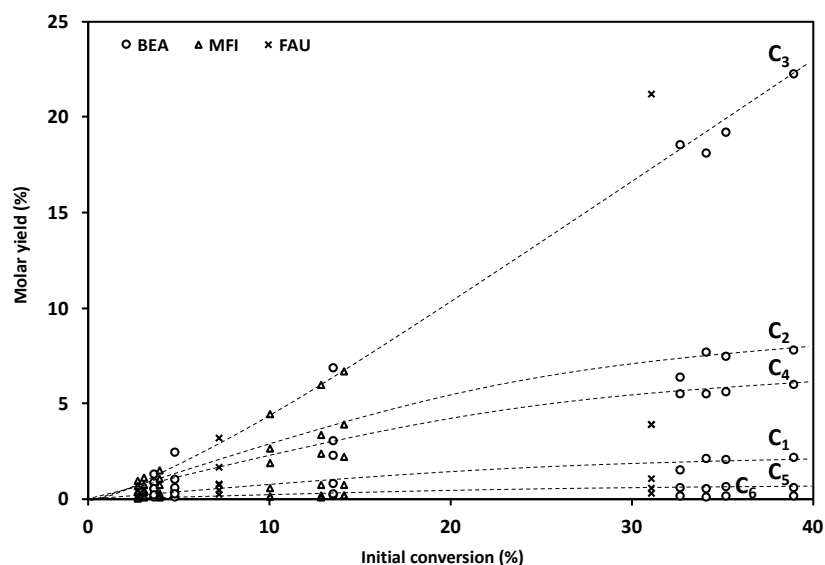


Figure B1. *n*-hexane cracking on different catalysts series: FAU, *BEA and MFI. Initial yields into cracking products as a function of initial *n*-hexane conversion. Operating conditions: T = 813 K, P = 1 atm, $P_{N_2}/P_{n-c6} = 9$.

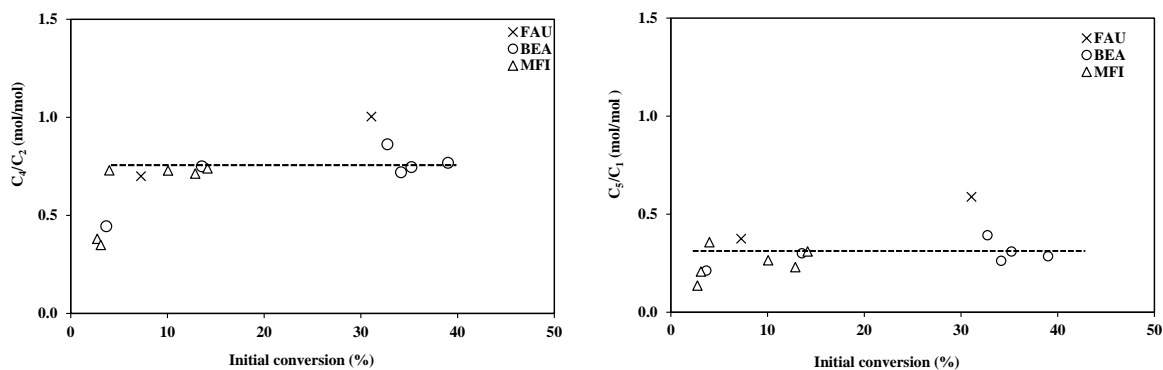


Figure B2. C_4/C_2 and C_5/C_1 molar ratios as a function of initial conversion of *n*-hexane cracking on different catalysts series: FAU, *BEA and MFI. Operating conditions: T = 813 K, P = 1 atm, $P_{N_2}/P_{n-c6} = 9$.

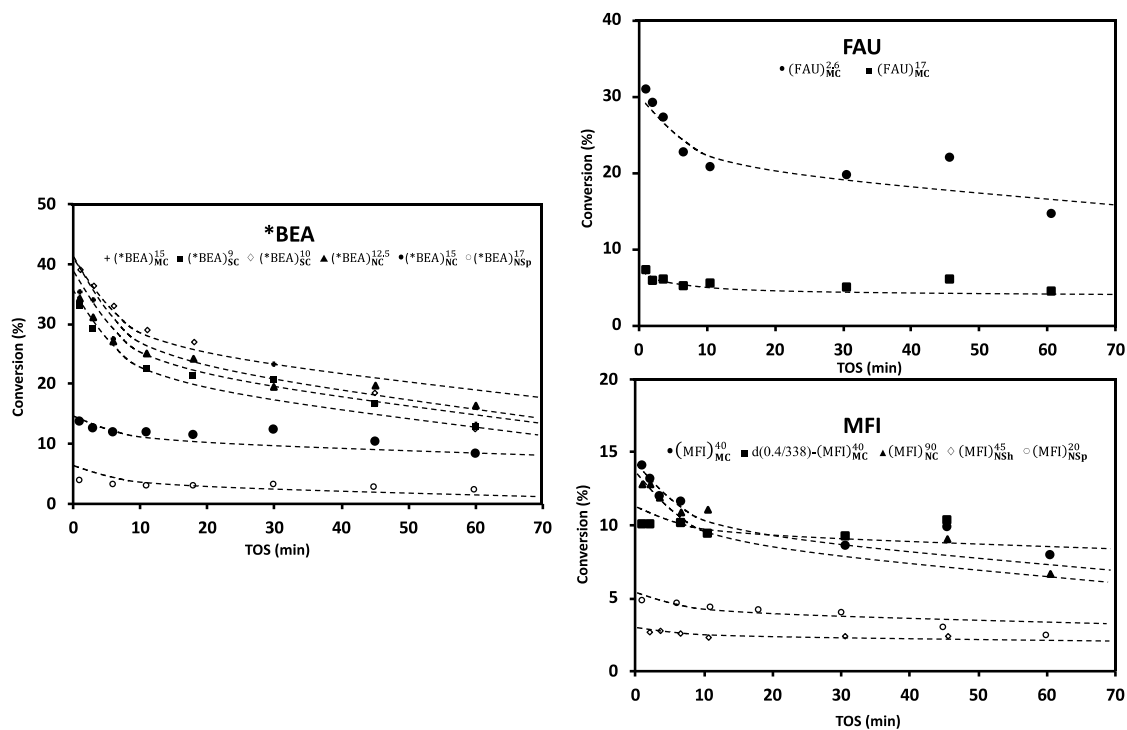


Figure B3. *n*-Hexane conversion as a function of time of stream (TOS). Operating conditions: $T = 813 \text{ K}$, $P = 1 \text{ atm}$, $P_{\text{N}_2}/P_{\text{n-c6}} = 9$.

Table B1. Initial activity in *n*-hexane cracking obtained on Amberlyst[®] 15, and zeolites (commercial, modified and synthesized): MOR, FAU, *BEA and MFI.

Reaction conditions: *n*-hexane cracking: $T = 813 \text{ K}$, $P = 1 \text{ atm}$, $P_{\text{N}_2}/P_{\text{n-c6}} = 9$ and $\tau = 0.04 \text{ s}$

Catalyst	$A_{\text{n-c6}}^0$ ($\text{mol h}^{-1} \text{g}^{-1}$) $\times 10^2$	TOF ^a (h^{-1})
$\text{SiO}_2\text{-Al}_2\text{O}_3$	0.022	2
(FAU) _{SC} ^{2.6}	24	595
(FAU) _{SC} ¹⁷	5	254
(*BEA) _{MC} ¹⁵	27	360
(*BEA) _{SC} ⁹	25	500
(*BEA) _{SC} ¹⁰	30	372
(*BEA) _{NC} ^{12.5}	26	562
(*BEA) _{NC} ¹⁵	11	370
(*BEA) _{NSp} ¹⁷	3	291
(MFI) _{MC} ⁴⁰	11	361
(MFI) _{NC} ⁴⁵	10	301
(MFI) _{NSh} ⁴⁵	2	241
(MFI) _{NSp} ²⁰	3	199

^aTurnover frequency per Brønsted acid sites probed by the pyridine at 423 K

Table B2. Reference catalysts used in the laboratory drawn from [64].

Zeolite	Origin^a	Si/Al_{total}	BAS ($\mu\text{mol g}^{-1}$)	LAS ($\mu\text{mol g}^{-1}$)	TOF (h^{-1})
*BEA	C	12.0	463	352	
*BEA	M (desilication)	7.6	267	275	348
*BEA	M (desilication)	9.0	334	442	392
*BEA	C	11.8	346	349	430
*BEA	M (desilication)	8.6	295	446	406
*BEA	S	35.0	523	99	355
*BEA	M (desilication)	26.8	285	190	375
*BEA	M (desilication)	28.9	362	137	357
*BEA	M (desilication)	29.1	431	168	357
MFI	C	90	112		275
MFI	M (desilication)		472		358

C: commercial, S: synthesized, M: modified, N.P. non published results.

Section C: etherification of glycerol with *tert*-butyl alcohol

C.M.1. Method for calculation of the effectiveness factor from two crystal sizes and two catalyst activities.

The initial rate can be simplified in respect to a TBA/GLY ratio of 4 as follows:

$$r_{A,0} = 4k[GLY]_0^2 \quad (C10)$$

- The expression of Thiele modulus for reaction order of n [1]

$$\phi_s = \sqrt{\frac{n+1}{2}} L \sqrt{\frac{kC^{n-1}}{D_e}} \quad (C11)$$

with, L : crystal size (nm), k : intrinsic kinetic constant (mol/m³ cat.s), and D_e : effective diffusion (m²/s)

- Effectiveness factor:

$$\eta = \frac{\text{(actual mean reaction rate within pore)}}{\text{(rate if not slowed by pore diffusion)}} = \frac{r_{A, \text{ with diffusion}}}{r_{A, \text{ without resistance}}} \quad (C12);$$

where for the shape here considerate,

$$\eta = \frac{1}{\phi_s} \left(\frac{1}{\tanh 3\phi_s} - \frac{1}{3\phi_s} \right) \quad (C13)$$

- Combining (C1) and (C12):

$$\phi_s = \sqrt{\frac{3}{2}} L \sqrt{\frac{\eta k}{[GLY]_0^2 D_e}} \quad (C14)$$

- Assumption: the same zeolite framework leads to identical k and D_e

If two crystal sizes L_1 and L_2 and two kinetic rates (k_{a1} and k_{a2}), are known, then,

$$\Rightarrow \frac{\phi_{s1}}{\phi_{s2}} = \frac{L_1}{L_2} \quad (C15)$$

$$\Rightarrow \frac{r_{A1}}{r_{A2}} = \frac{\eta_1}{\eta_2} \quad (C16)$$

The solution becomes possible with this algebraic loop resolved by iteration [65]. For that we begin by an arbitrary value of η_1 (e.g. 0.7), and solve the system by using the loop up to convergence. With this method, it is no need to have the value of $r_{\text{intrinsic}}$ to calculate the Thiele modulus and the efficiency factor.

[1] Wijngaarden R.J., Kromberg A., Westerrterp K.R., Industrial Catalysis : Optimizing catalysts and Processes,(1998) Wiley-VCH

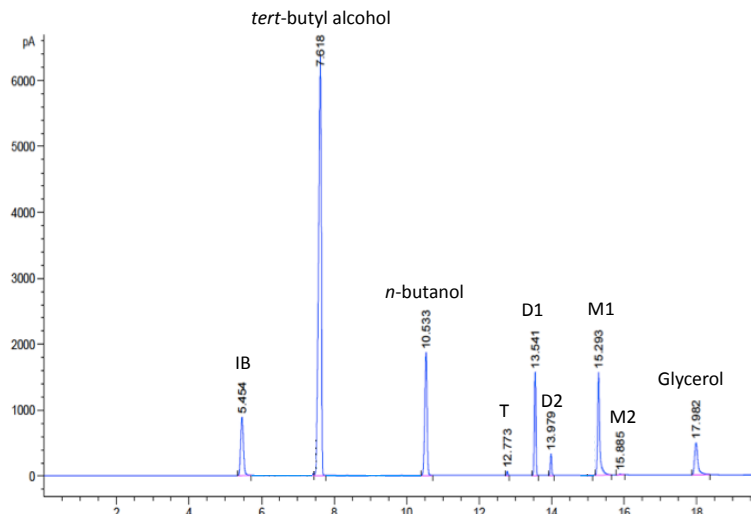


Figure C1. Typical chromatogram for the etherification of glycerol with *tert*-butyl alcohol; M1: 3-*tert*-butoxy-1,2 propanediol, M2: 2-*tert*-butoxy-1,3 propanediol, D1: 1,3-di-*tert*-butoxy-2-propanol, D2: 2,3-di-*tert*-butoxy-1-propanol, T: tri-*tert*-butoxy-propane, IB: isobutylene. *n*-butanol as internal standard.

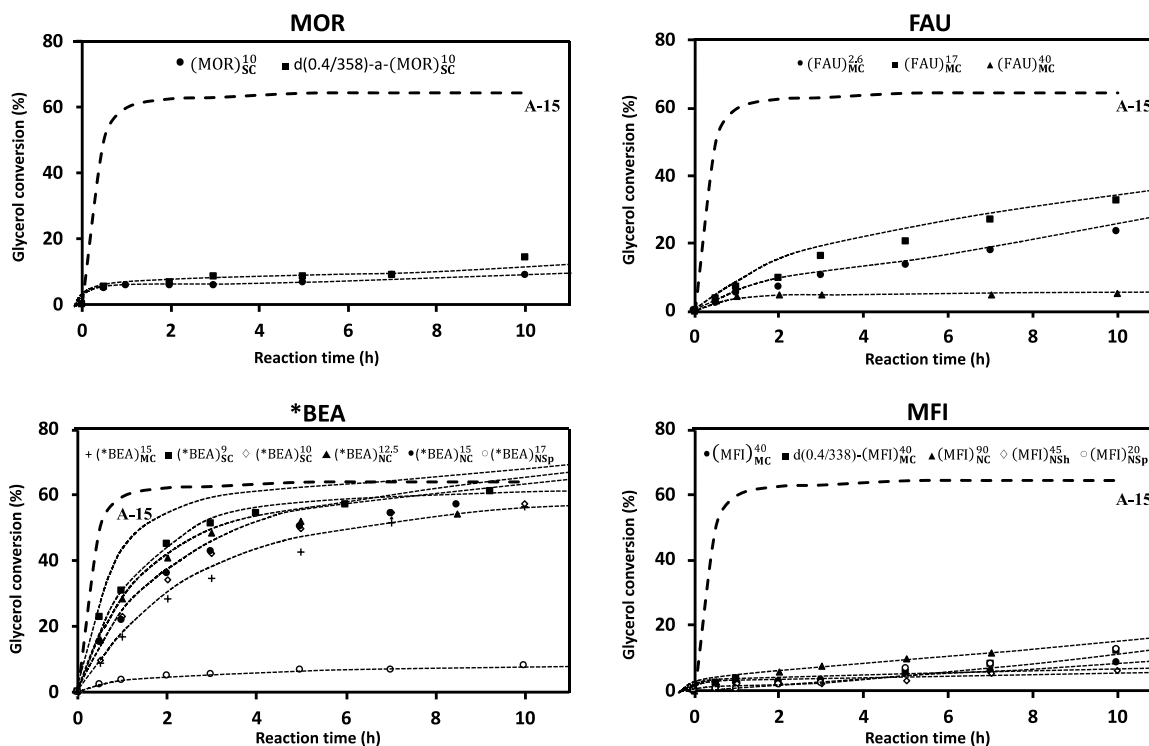


Figure C2. Glycerol conversion as a function of reaction time at 363 K, 1200 rpm, autogenous pressure, 7.5% of catalyst and glycerol/*tert*-butyl alcohol molar ratio of 0.25.

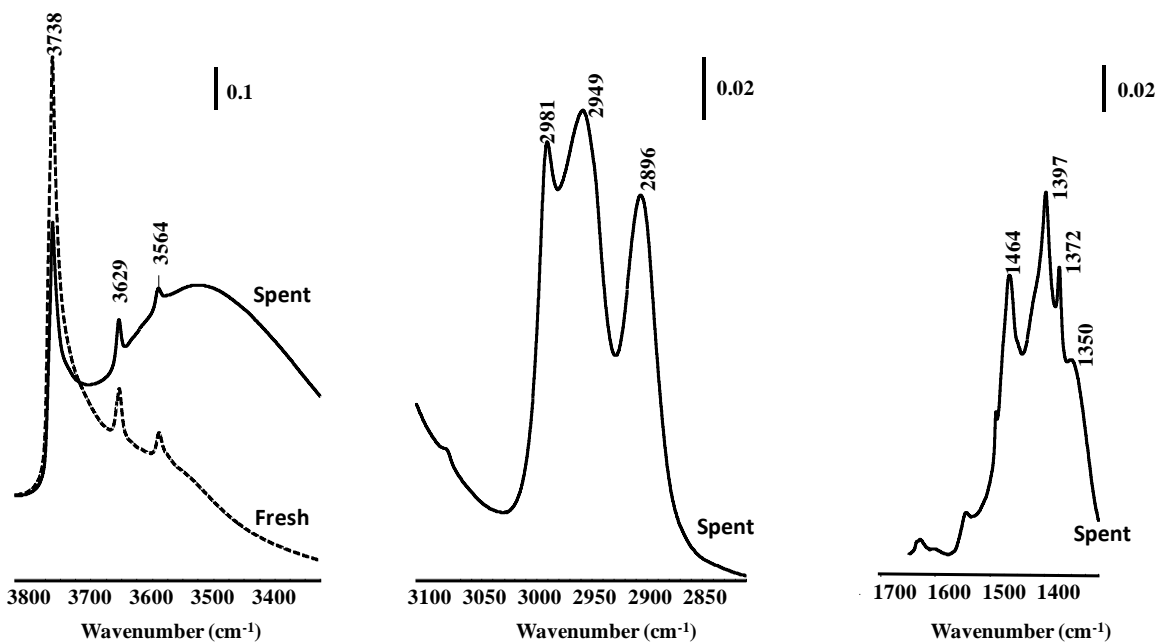


Figure C3. FT-IR spectra of: fresh and spent (after rinsing with ethanol) zeolite (FAU)₄₀^{SC}.

Table C1. Thermodynamic data.

Name	G° kJ. mol ⁻¹	Origin
MTBG	-394.97	Gani method
DTBG	-336.49	Gani method
TTBG	-269.49	Gani method
TBA	-177.6	database
G	-447.1	database
H ₂ O _(l)	-237.2	database
IB _(g)	58.08	database

Table C2. Selectivity of glycerol monoethers (MTBG), glycerol diethers (DTBG) and glycerol triether (TTBG) at isoconversion. ($X \approx 20\%$) obtained on MOR, FAU, *BEA and MFI catalysts.

Catalyst	X (%)	MTBG (%)	DTBG (%)	TTBG (%)
(FAU) ₁₇ ^{SC}	20	87	12.6	0.4
(FAU) ₄₀ ^{SC}	23	83	16.4	0.6
(*BEA) ₉ ^{SC}	22	97	3	0
(*BEA) ₁₀ ^{SC}	23	98	2	0
(*BEA) _{12.5} ^{NC}	22	89	11	0
(MFI) ₄₅ ^{NC}	20	99	1	0

Glycerol etherification: 7.5 wt.% of catalyst to glycerol mass, glycerol/*tert*-butyl alcohol molar ratio = 0.25, T = 363 K.